

# Modeling and Optimization of PEMFC Systems and its Application to Direct Hydrogen Fuel Cell Vehicles

September 9, 2008

Hengbing Zhao and Andrew F. Burke

## Table of Contents:

Abstract.....	2
1 Introduction.....	2
2 The Fuel Cell System and Fuel Cell Vehicles.....	4
2.1 Fuel Cell System.....	4
2.2 Fuel Cell Vehicle.....	5
3 System Sizing, Modeling, and Optimization of Operating Conditions.....	6
3.1 Quasi-Steady State Fuel Cell System Optimization Model.....	6
3.2 Sizing of Auxiliary Subsystems.....	8
3.3 Considerations in the Optimization Model.....	9
3.4 Search for Optimum Operating Conditions.....	12
3.5 Optimal Operation and Comparison with Conventional fixed back pressure Operation.....	14
4 Dynamic Modeling and Control.....	20
4.1 Dynamic Compressor Model and Control.....	21
4.2 Lumped Manifold/Cathode Model.....	23
4.3 Cooling/Humidifier and Throttle Control.....	25
4.4 Fuel Cell Model.....	27
5 Fuel Cell System and Vehicle Simulation Results.....	28
5.1 Results for the Dynamic Fuel Cell System.....	28
5.2 Simulation Results of Fuel Cell Vehicles.....	34
6 Conclusions and Discussion.....	39
Acknowledgements.....	41
References.....	41
Appendix 1.....	44
Unit Conversion Correction of the Former Optimization Model.....	44
Appendix 2.....	45
Effect of Humidification on the Mass Flow.....	45
Appendix 3.....	49
Change of the Air SR Calculation in the Quasi-Steady Fuel Cell System.....	49
Appendix 4.....	50
Traction Motor Controller.....	50
Appendix 5.....	51
Operation Instructions for Fuel Cell System and Fuel Cell Vehicle Models.....	51
Tables of Figures.....	52
Tables.....	53

# Modeling and Optimization of PEMFC Systems and its Application on Direct Hydrogen Fuel Cell Vehicles

## Abstract

Proton Exchange Membrane fuel cell (PEMFC) technology for use in fuel cell vehicles and other applications has been extensively developed in recent decades. Besides the fuel cell stack, air and fuel control, and thermal and water management are major challenges in the fuel cell vehicle development. The air supply system can have a major impact on overall system efficiency. In this report, a fuel cell system model for optimizing system operating conditions was developed which includes the transient dynamics of the air system with varying back pressure. The model is scalable so that it can be used to simulate the operation of an arbitrary size (power) fuel cell. Finally, the model is applied as part of a dynamic forward-looking vehicle model of a load-following direct hydrogen fuel cell vehicle to explore the energy economy optimization potential of fuel cell vehicles.

**Keywords:** fuel cell system; direct hydrogen fuel cell vehicle; optimization model; quasi-steady; dynamic; simulation

## 1 Introduction

In recent decades hydrogen Proton Exchange Membrane fuel cell (PEMFC) technology for use in fuel cell vehicles has been extensively developed by major auto companies. Compared with internal combustion engine vehicles, the hydrogen fuel cell vehicle has the advantages of high energy efficiency and low emissions due to the direct conversion of chemical energy into electricity without combustion. Compared with the battery electric vehicles, it has the advantages of a longer driving range and short refueling time. For these reasons, hydrogen fuel cells can become the favored propulsion system for most classes of vehicles in the future. However, it is likely that the use of fuel cells in vehicles is still far in the future due to the high cost of fuel cells, their limited durability and the public availability of hydrogen fuel [1].

The application of fuel cells in automobiles is particularly difficult because of the rapidly varying power demand typical of those applications. The fuel cell system, consisting of the stack, air and fuel supply, and water and thermal management subsystems, is usually designed around its maximum power operating point even though it operates most often

at much lower power. Hence it is necessary to be able to operate the fuel cell system at high efficiency over a wide power range. Hence, in automotive applications, the fuel cell systems has to be able to adapt to critical operating conditions such as frequent start-up and stop, sudden load changes, and varying power levels. Improper system design and control can cause air/fuel starvation, flooding, membrane drying, and pressure imbalance across the membrane, which will damage the fuel cell stack. Therefore, there is a need to develop a tool to optimize the fuel cell system operation over the full load range to attain high fuel economy and to assess the transient response of the fuel cell system and its impact on the performance of fuel cell vehicles using appropriate control strategies.

Much work has been done in the past to model fuel cell systems, optimize the operating conditions, and simulate fuel cell vehicles. Fuel cell models at the cell level are presented in [2,3,4]. Studies concerned with optimum operating conditions are discussed in [5,6,7,8,9,10,11,12]. The characteristics of low pressure and high pressure fuel cell systems are addressed with regard to the system efficiency and transient response in [7,13,14]. Lumped filling/emptying dynamic fuel cell models are presented in [15,16,17]. Air supply control strategies and analyses based on dynamic quasi-steady fuel cell operation are described in [15,18,19,20, 21, 22]. These studies established a good foundation for understanding fuel cell systems and fuel cell vehicles. However, the above models were developed for a specific fuel cell system or without considering the design of the stack, sizing of the system, or optimization of operating conditions. In addition, the models did not treat the transient dynamics of the system and its effect on system efficiency. A fuel cell system optimization model which describes on a controls basis the transient dynamics of the system and is applicable to a generic fuel cell design (scalable to fuel cells of arbitrary power) is needed for evaluating the fuel cell system in vehicles of various classes and for exploring the energy economy of those vehicles. The development and application of such a model are the subjects of this report.

This report focuses on system sizing, optimization, dynamic modeling and control of the fuel cell system and its application to direct hydrogen fuel cell vehicles. A scalable fuel cell system optimization model with consideration of the design parameters of the fuel cell stack is developed with the objective of maximizing the system efficiency and net output power. Based on the optimal mass flow and back pressure, a lumped filling/emptying dynamic model is developed for investigating the transient effect of air supply on the fuel cell system performance. The dynamic fuel cell system model is then integrated into a dynamic forward-looking vehicle model of a load-following direct hydrogen fuel cell vehicle to analyze the transient effect of the fuel cell system on the vehicle performance and fuel economy ( $\text{kgH}_2/\text{km}$ ).

In Section 2 of the report, the fuel cell system and its integration into a fuel cell vehicle is described. A quasi-steady optimization model and related transient dynamic model of the fuel cell system are described in sections 3 and 4, respectively. Simulation results of the fuel cell system and fuel cell vehicles are presented in section 5. The conclusions are summarized in section 6.

## 2 The Fuel Cell System and Fuel Cell Vehicles

### 2.1 Fuel Cell System

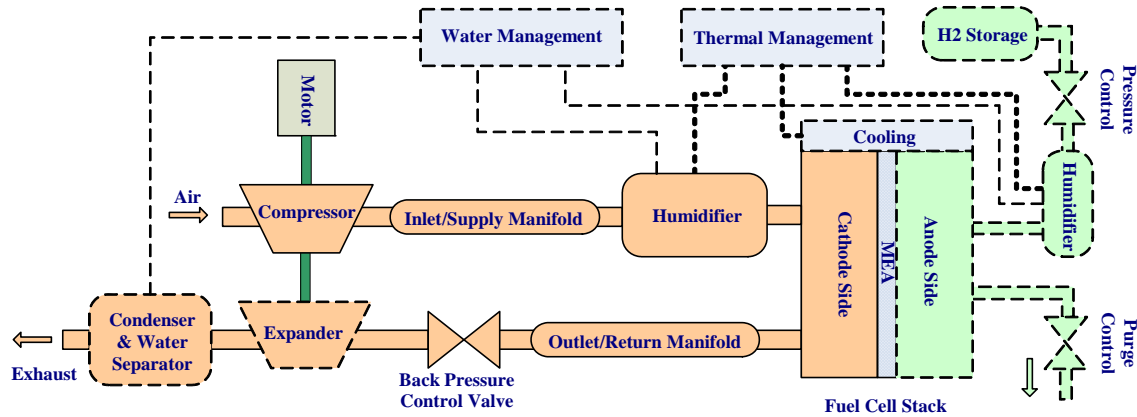
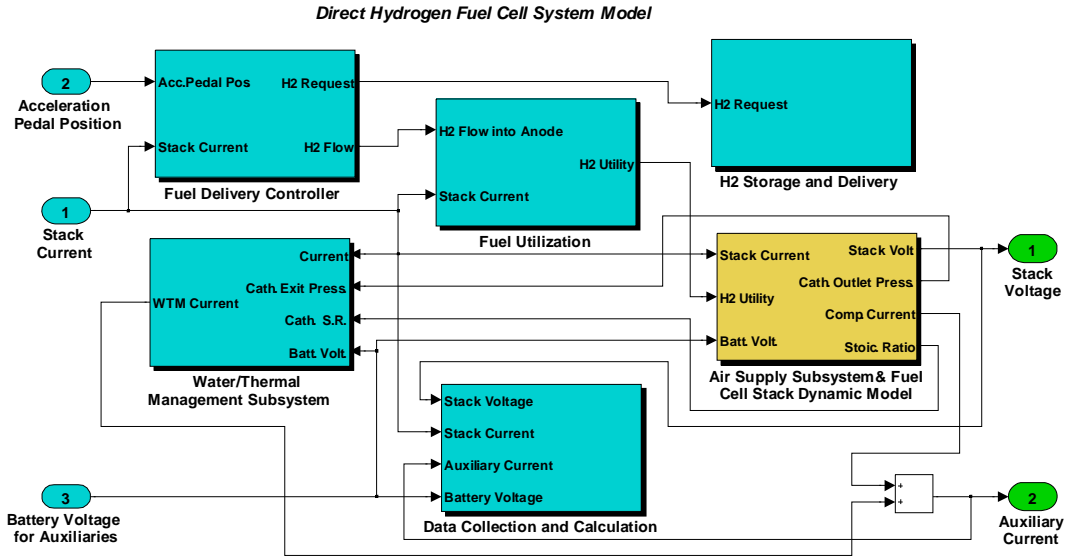


Figure 1 Direct hydrogen fuel cell system Schematic Diagram

A fuel cell stack is the heart of a fuel cell system. However, without auxiliary components such as air compressor, humidifiers and regulators, the stack itself could not function. The fuel cell system configurations can vary significantly depending on the application. As shown in Figure 1, a direct hydrogen fuel cell system for a vehicle typically involves the following five subsystems: air supply and control, fuel supply and control, fuel cell stack, water management, and thermal management. The air supply subsystem includes the air compressor and expander, supply manifold, cathode side of the fuel cell stack, return manifold, and back pressure control valve. The fuel supply subsystem consists of a high pressure fuel tank, pressure regulator, supply manifold, the anode side of the fuel cell stack, and purge control valve. The water management subsystem includes air/fuel humidifiers or vapor injector and vapor condenser. The thermal management consists of water or air cooling loop for the stack, and temperature control for humidifiers and radiator. The interaction of the four subsystems has a strong influence on the fuel cell stack performance.

The fuel cell system to be modeled is shown in Figure 2. The stack current is critical system variable and it is used to determine the hydrogen consumption in the stack. The optimum operating conditions such as mass flow, back pressure, and water and thermal management parameters, obtained from the quasi-steady fuel cell system optimization model, are used in the transient dynamic model. The optimal air mass flow is achieved through a combination of feedback and feed forward control of the compressor. The back pressure of the stack is controlled by adjusting the opening area of the throttle through a feedback and feed forward controller. In other words, the fuel cell system is controlled to operate around its optimum operating conditions.



**Figure 2** Diagram of the fuel cell system for direct hydrogen fuel cell vehicles

The fuel cell system is complex and care must be taken to understand the level of model complexity needed to adequately account for the impact each of the components on the overall system performance and efficiency. The transient phenomena of the electrochemical reactions in the stack can be ignored due to their fast response. The response of the water and thermal management subsystem is much slower. Hence, the stack and humidifier temperature change slowly and can be considered to be constant. The hydrogen is stored in a high pressure tank. Its dynamics is fast and can be neglected relative to the air supply from the compressor. Therefore, only dynamics related to the air supply subsystem are likely to have a large impact on the system performance and are considered in the present model. With regard to the parasitic losses, the parasitic loss of the air supply system is about 80 percent of the total losses. As a result, the air supply subsystem has a dominant impact on the system efficiency. The smaller parasitic losses from the water and thermal management subsystems are scaled from those given in [6] and used in the quasi-steady optimization model.

## 2.2 Fuel Cell Vehicle

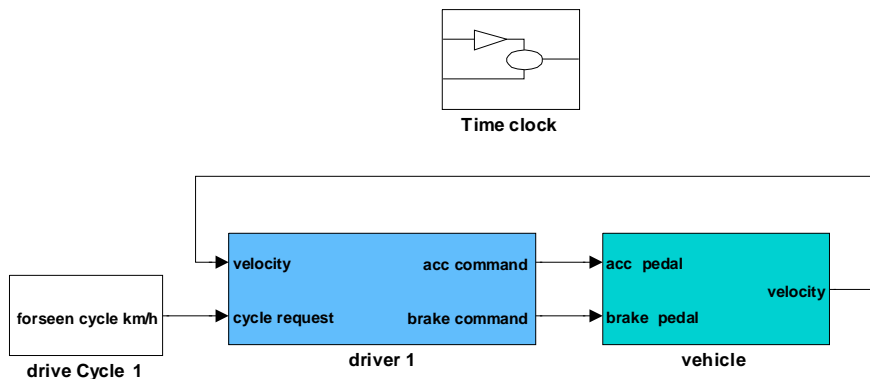


**Figure 3** Driver end of the direct hydrogen fuel cell vehicle model

The dynamic fuel cell system model was integrated into a forward-looking vehicle model of a load-following direct hydrogen fuel cell vehicle. The driver end of the fuel cell vehicle model shown in Figure 3 consists of three main blocks: drive cycle, driver, and vehicle. The detailed fuel cell vehicle model can be found in [21,22]. The drive cycle block defines the driving profile in the terms of velocity vs. time. The driver block represents the driver characteristics, generating the acceleration and brake commands to the vehicle block according to the driving cycle and the actual vehicle velocity. The vehicle block includes vehicle road load parameters, motor and transmission characteristics, and fuel cell system. The motor and transmission subroutines generate the current demand for the fuel cell system. Vehicle operation on various drive cycles such as FUDS, US06, HIWAY, JP1015, ECE, and NEDC can be simulated with the models.

In a fuel cell vehicle, the hydrogen fuel may not be fully utilized. For closed end hydrogen fuel cell systems, frequent purging is used to remove the accumulated water vapor and the nitrogen diffused through the membrane. For open end hydrogen systems, a pump is employed to circulate the unused hydrogen. However, compared to the power provided to air supply system and cooling system, the power consumption of the hydrogen fuel supply system is small and can be neglected.

### **3 System Sizing, Modeling, and Optimization of Operating Conditions**

The fuel cell stack can deliver electricity with high efficiency. However, the operation of the on-board auxiliaries can strongly affect the performance of fuel cell systems. A quasi-steady fuel cell system optimization model was developed by the fuel cell vehicle modeling group at ITS-UCD [22]. The model, employing PEMFC data from [3], was developed to analyze different air supply configurations and their tradeoffs and search for the optimum operating conditions to maximize the net system power and system efficiency with consideration of the water and thermal management. The quasi-steady optimization model in this report was developed starting from the original model adding further consideration of the channel flow field design, sizing of the air supply and other subsystems, and the impact of the humidification and oxygen consumption on the pressure loss in the stack.

#### ***3.1 Quasi-Steady State Fuel Cell System Optimization Model***

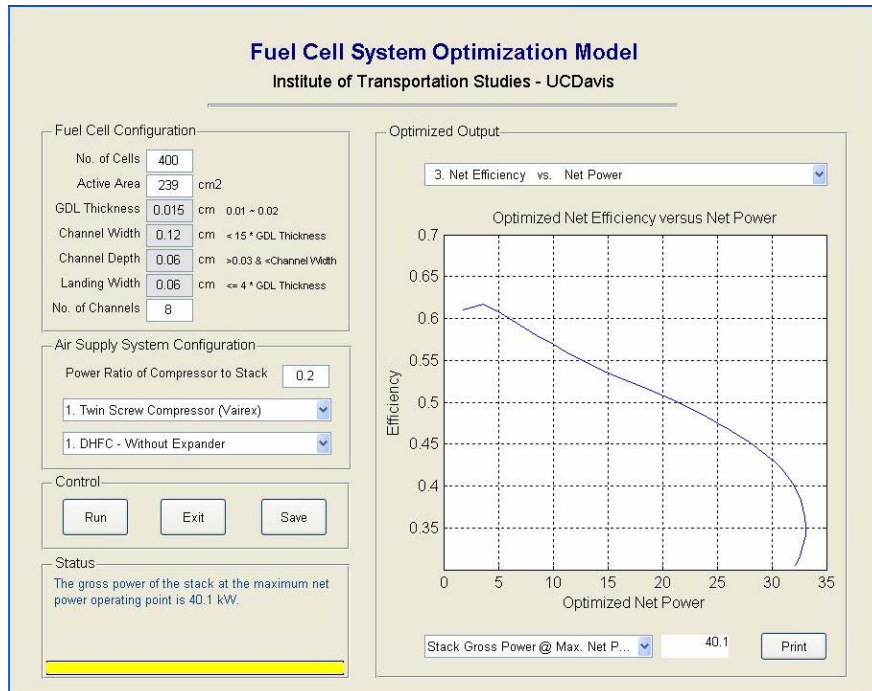


**Figure 4 Interface of the fuel cell system optimization model**

The GUI of the quasi-steady fuel cell system optimization model is shown in Figure 4. The interface gives some system parameters which affect the system optimization results. The fuel cell performance is sensitive to the mass flow of the reactants, which depends on the fuel cell stack design, which is described in terms of the following parameters: the number of cells, the active area of the cell, and flow field design including the channel shape, dimensions and spacing. These parameters play a key role in determining the pressure drop across the stack and the parasitic loss of the air supply system. The thickness of the gas diffusion layer (GDL) is a key variable for designing the flow field. The width of the flow channel and landing area (channel spacing) is limited to the thickness of the GDL due to the mechanical strength of GDL. The number of the flow paths and the active area in the flow field plate determines the equivalent flow path length. The pressure drop due to friction through the flow field can be adjusted by varying the channel design parameters. The pressure drop across the stack is the sum of the pressure drop through the channel flow field and the pressure drop in the vertical inlet and outlet manifold. The quasi-steady power consumption of the compressor depends on the mass flow, pressure drop across the stack and the back pressure of the stack. The objective of the flow field plate design is to minimize the pressure drop across the stack at the nominal operating point while avoiding flooding. In the optimization model, only rectangular flow channels are considered.

The ratio of the maximum compressor power to the rated stack power is introduced as the scaling factor for the air compression system. The scaling factor used in the present analysis is .15-.20. The performance map for the compressor system has been scaled from that of a 17 kW Vairex twinscrew compressor and a 21 kW Solectria induction motor and controller combination.

Temperature, relative humidity, operating pressure and the air mass flow are the four key external system variables that have a major impact on the performance of the fuel cell stack. Assuming the stack temperature and the relative humidity are well controlled, the operating pressure and the air mass flow will determine the oxygen partial pressure at the cathode catalyst layer and consequently the cathode overpotential voltage. The average pressure in the stack is used to calculate the effect of the water vapor on the mass flow rate. The water and thermal management losses are scaled from the reference system previously analyzed in [6].

### 3.2 Sizing of Auxiliary Subsystems

The auxiliary subsystems including the air compression subsystem and the water and thermal management subsystem are sized based on the rated fuel cell stack power. The rated stack power is calculated based on the stack cell number, active area, and the polarization curve of the MEA.

$$P_{stack} = V_{cell} \cdot J_{cell} \cdot A_{cell} \cdot n_{cell} \quad (1)$$

where  $V_{cell}$  is the cell voltage at the current density of  $J_{cell}$ ,  $A_{cell}$  is the active area of the cell, and  $n_{cell}$  is the number of cells.  $V_{cell} = 0.5V @ J_{cell} = 900 \text{ mA/cm}^2$  is used to estimate the rated stack power.

The ratio of the compressor power to the stack power,  $k$ , is introduced to size the air compression system. In most system designs, the power of the air compressor is about 15~20% of the stack power. The required maximum power of the drive motor and the compressor can be expressed as

$$P_{motor} = k \cdot P_{stack} \quad (2)$$

$$P_{comp} = P_{motor} \cdot \eta_{motor} \quad (3)$$

where  $\eta_{motor}$  is the combined efficiency of the drive motor and controller. A Vairex twinscrew compressor and a Solectria induction motor and controller combination are employed in the optimization model. The maximum power points of the drive motor and the compressor,  $P_{motor,0}$  and  $P_{comp,0}$ , are based on their performance maps. The scaling factors for the motor and the compressor maps are given by

$$k_{motor} = \frac{P_{motor}}{P_{motor,0}} \quad (4)$$

$$k_{comp} = \frac{P_{comp}}{P_{comp,0}} \quad (5)$$

Thermal and water management for fuel cells are challenging issues in automotive applications. A fuel cell system operates at low temperature compared to an engine and as result requires a larger radiator. A condenser is needed for recovering the water formed in the fuel cell for humidifying the inlet reactant gases. The losses from the coolant pump, radiator fan and condenser are small compared to the loss from the air compression subsystem. The water and thermal management losses are derived from [6] by scaling them based on the stack power.

### 3.3 Considerations in the Optimization Model

In the original fuel cell optimization model [11], only the dry air mass flow was considered for calculating the pressure drop in the channel flow field. The effect of the humidification and the oxygen consumption on the air mass flow was not considered (Only the change of the density of the humid air was considered). The saturated water vapor pressure is a function of only temperature and is 0.46733 atm. at 80 °C. The change of the air mass flow caused by humidification is significant and should be considered in the model.

The dry air mass flow in the stack decreases due to the electrochemical reaction. The oxygen, nitrogen and hydrogen diffusion through the membrane is small and its effect on the mass flow is neglected here. The outlet dry air mass flow is expressed as

$$\begin{aligned} \dot{m}_{air,outlet} &= \dot{m}_{air,inlet} - \frac{\dot{m}_{air,inlet}}{M_{air,inlet}} \cdot x_{on} \cdot \frac{1}{SR} \cdot M_{O_2} \\ &= \left( 1 - \frac{x_{on} \cdot M_{O_2}}{SR \cdot M_{air,inlet}} \right) \dot{m}_{air,inlet} \end{aligned} \quad (6)$$

where  $M_{air,inlet}$  is the mole mass of the dry air at the inlet,  $\dot{m}_{air,inlet}$  the inlet dry air mass flow rate, and  $x_{on}$  the mole ratio of oxygen and dry air. The ratio of the dry air mass flow at the outlet and at the inlet vs. the stoichiometric ratio (SR) is shown in Figure 5. The effect of the consumed oxygen on the change of the dry air mass flow should not be neglected when the SR is less than 2.0. (Usually the optimal SR from the optimization model is less than 2.)

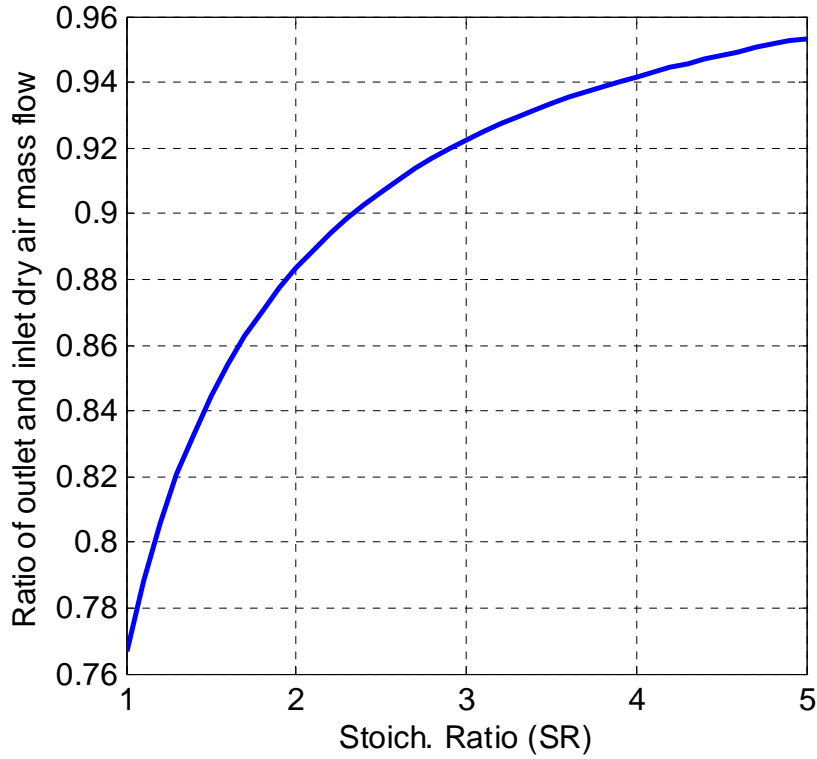


**Figure 5 Mass flow ratio of the outlet and inlet dry air flow vs. SR**

The molar molecular weight of the exhaust dry air also changes due to the oxygen consumption as shown in equation (7) and Figure 6.

$$M_{air,outlet} = \frac{x_{on} \frac{SR-1}{SR}}{1-x_{on} \frac{1}{SR}} M_{O_2} + \frac{1-x_{on}}{1-x_{on} \frac{1}{SR}} M_{N_2} \quad (7)$$

The plot shows that the change of the molar molecular weight of the exhaust dry air changes with SR. However, the change of the molecular weight is less than 2 percent and can be neglected in the optimization model when the SR is less than 2. Hence it is assumed

$$M_{air,outlet} \cong M_{air,inlet} = M_{air} \quad (8)$$

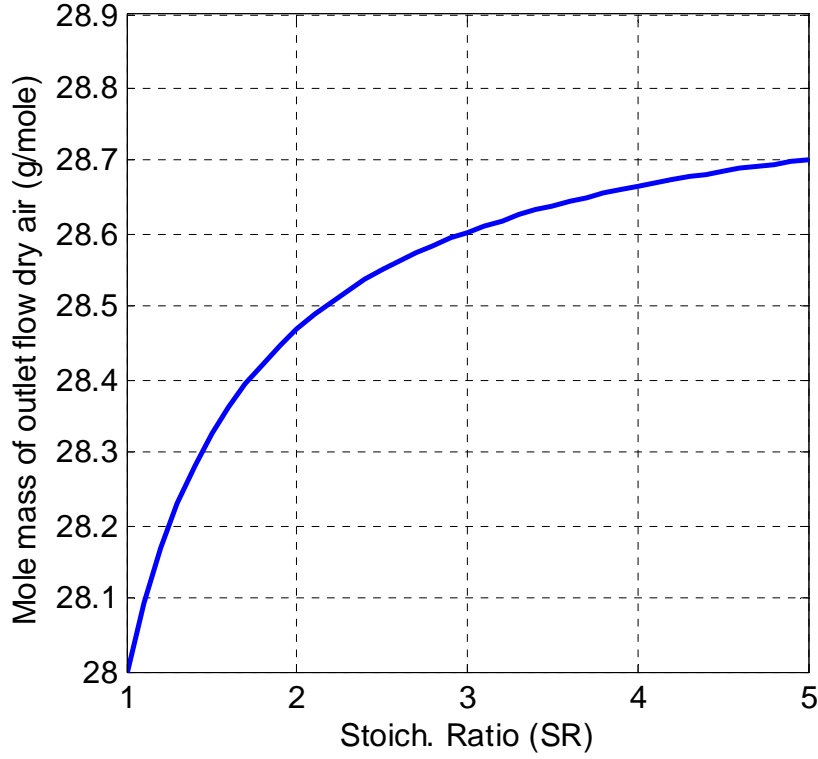


Figure 6 Outlet flow dry air mole mass vs. SR

The vapor mass flow contributes significantly to the stack pressure loss. It is related to the dry air mass flow, pressure drop, and the back pressure using the ideal gas law. The maximum pressure drop across the stack for the optimal operation (varying SR and varying back pressure) is 0.4 atm. The average pressure from the back pressure and estimated pressure drop in the stack is used to calculate the water vapor mass flow. The averaged mass flow in the stack is then used to calculate the pressure loss in the optimization model. The average humid air mass flow in the stack is derived in Appendix 2 and expressed as

$$\begin{aligned}
 \dot{m}_{average} &= \frac{\dot{m}_{inlet} + \dot{m}_{outlet}}{2} \\
 &= \frac{1}{2} \left[ \left( \frac{P_{vapor}}{P_{inlet} - P_{vapor}} \cdot \frac{M_{vapor}}{M_{air}} + 1 \right) + \left( \frac{P_{vapor}}{P_{outlet} - P_{vapor}} \cdot \frac{M_{vapor}}{M_{air}} + 1 \right) \cdot \left( 1 - \frac{x_{on} \cdot M_{O2}}{SR \cdot M_{air}} \right) \right] \cdot \dot{m}_{air,inlet} \quad (9)
 \end{aligned}$$

where,  $\dot{m}_{air,inlet}$  is the dry air mass flow at the inlet,  $P_{vapor}$  the water vapor partial pressure,  $P_{inlet}$  the inlet pressure,  $P_{outlet}$  the outlet pressure,  $M_{air}$  the air molecular weight, and  $M_{vapor}$  is the water vapor molecular weight.

### 3.4 Search for Optimum Operating Conditions

The pressure drop across the stack is related to the humid air mass flow, stack back pressure, and flow field plate design. The pressure loss in the flow channel can be obtained by the Darcy-Weisbach Law. However, the vapor mass flow in the channel is related to the back pressure and the pressure drop on the channel. In the optimization model, the maximum allowable pressure drop across the stack and the assumed flow path number (channel number) are given. First, the humid air flow rate is calculated with the back pressure, the dry air mass flow rate, and the interpolated pressure drop from the maximum allowable pressure drop. The actual pressure drop across the stack is obtained by the Darcy-Weisbach Law. The model calculates for every possible triplet (the current density,  $J$ , the dry air mass flow,  $\dot{m}_d$  and the back pressure,  $P_r$ ) the net output power of  $P_{net}(J, \dot{m}_d, P_r)$ . Then it searches among those which have  $P_{net}(J, \dot{m}_d, P_r) > 0$  and are within the safe operational region of the compressor to find the one with  $\max(P_{net}(J, \dot{m}_d, P_r))$ .

$$P_{net}(J, \dot{m}_{d,optimal}, P_{r,optimal}) = \max[P_{net}(J, \dot{m}_d, P_r)] \quad (10)$$

In other words, the optimal mass flow  $\dot{m}_{d,optimal}$  and back pressure  $P_{r,optimal}$  will yield the maximum net power for certain  $J$  values.

At the last step, the maximum actual pressure drop is obtained from the optimal results and compared with the input allowable pressure drop. If the maximum actual pressure drop on the stack matches the allowable pressure drop, the selected channel number and the optimum operating conditions are accepted. Otherwise, the channel number is changed and iteration continued until the maximum allowable pressure drop on the stack is matched. Figure 7 depicts the flowchart for optimizing the operating conditions and determining the channel number.

In order to compare the results for a fixed back pressure with those for the optimal conditions, the optimization model was modified to optimize the mass flow for the fixed back pressure operation. The channel number from the optimum solution (varying SR and varying back pressure) was used for the fixed back pressure calculation. Instead of changing the channel number, the allowable pressure drop is adjusted to match the maximum pressure drop in the stack for the optimal solution.

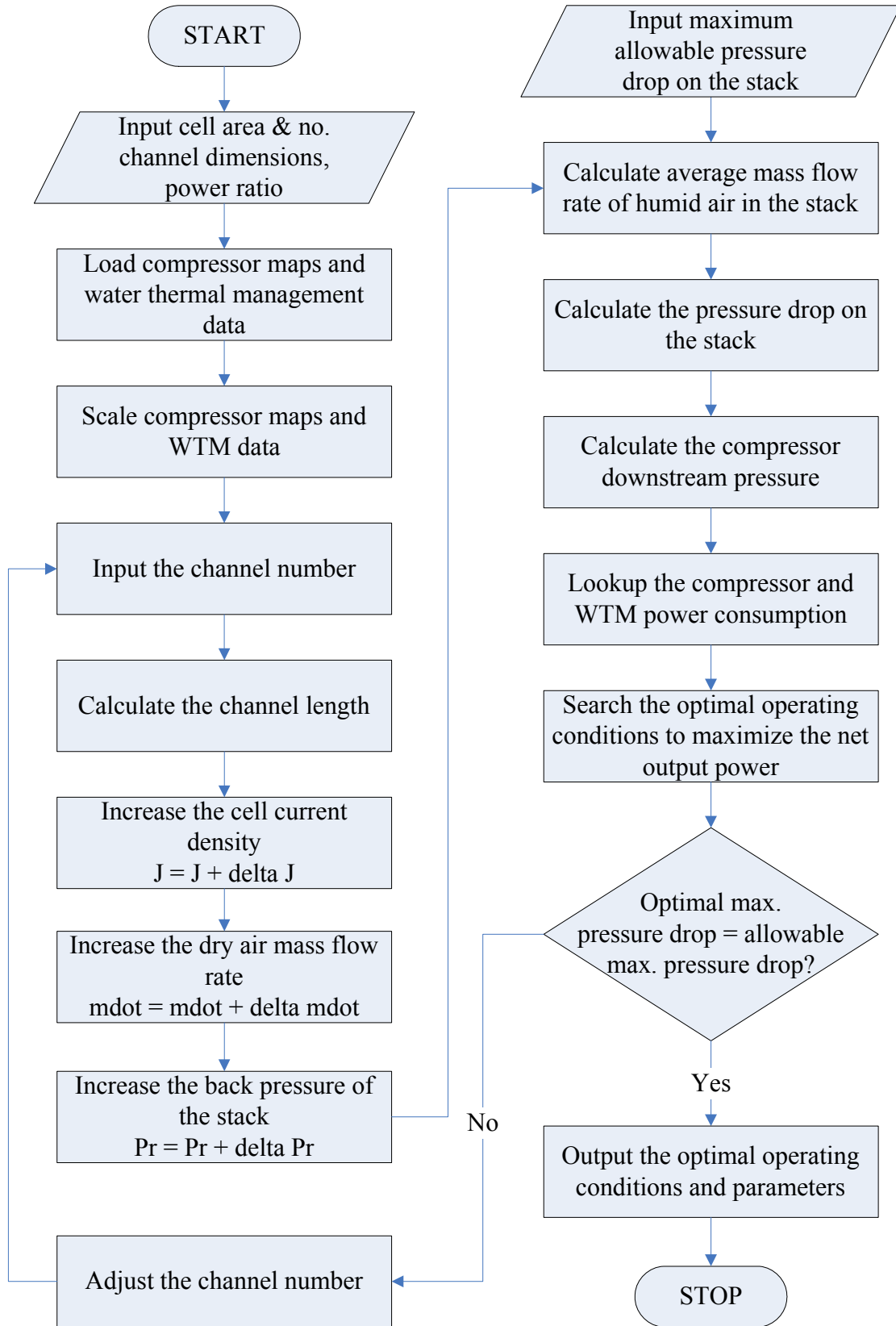


Figure 7 Flowchart of searching for the optimum operating conditions for the varying air stoich. number varying back pressure operation

### 3.5 Optimal Operation and Comparison with Conventional fixed back pressure Operation

The optimum operating conditions for the fuel cell system listed in Table 1 are presented in Figure 8. The maximum net power of 87.6 kW occurs at the current density of 825 mA/cm<sup>2</sup> with the back pressure of 1.8 atm. and the air SR of 1.6. The power of the stack, air compressor and radiator is 106.2 kW, 16.6 kW, and 1.9 kW, respectively. For comparison, the model was run for fixed back pressures of 2.0, 1.5, and 1.1 atm. Plots of the system efficiency for the various cases is shown in Figure 9. The polarization curves and the compressor responses for different operating modes are shown in Figure 10 and Figure 11, respectively. In addition, plots of the optimal net power, gross power, air SR, air mass flow rate, pressure drop across the stack, and the oxygen partial pressure at the catalyst layer vs. current density are presented in Figure 12-17.

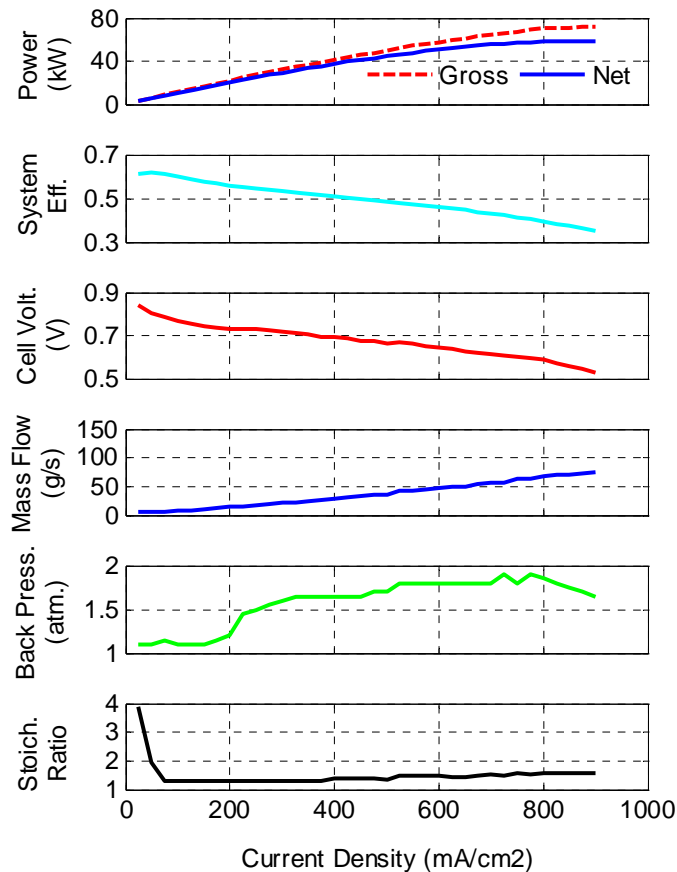
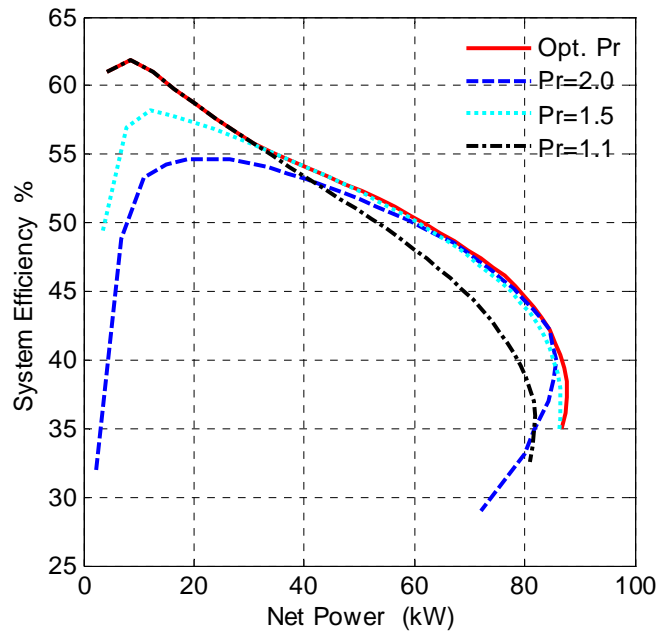


Figure 8 Optimum operating conditions for a direct hydrogen fuel cell system

**Table 1 Fuel cell stack and system parameters**

No. of Cells	440	Width of Flow Path (mm)	1.2
Active Area (cm <sup>2</sup> )	510	Depth of Flow Path (mm)	0.6
No. of Flow Paths	15	Width of Landing Area (mm)	0.6
Thickness of GDL (mm)	0.15	Power Ratio of Twin Screw Compressor to Stack	0.2



**Figure 9 Comparison of the system efficiency for different operating modes: optimal varying back pressure operation and fixed back pressure of 2.0, 1.5, and 1.1 atm.**

(Opt. Pr denotes optimal back pressure operation. Pr=2.0, Pr=1.5, and Pr=1.1 represent the fixed back pressure of 2.0 atm., 1.5 atm., and 1.1 atm., respectively.)

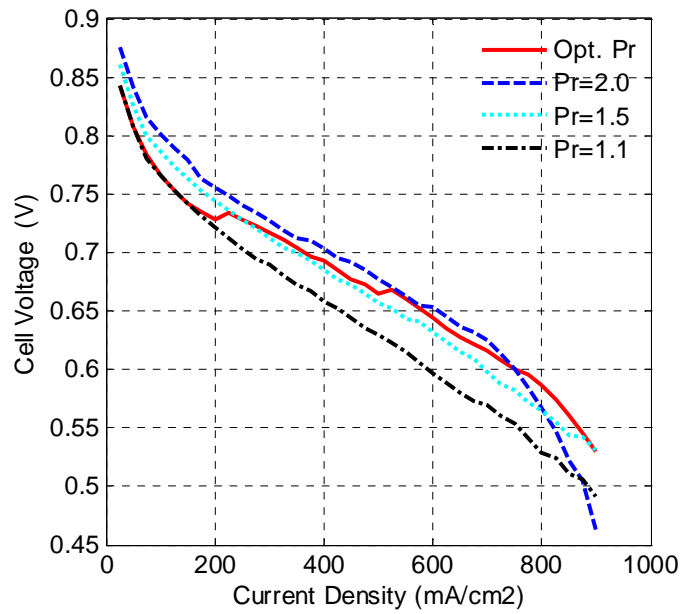


Figure 10 Optimal fuel cell polarization curves for different operating modes

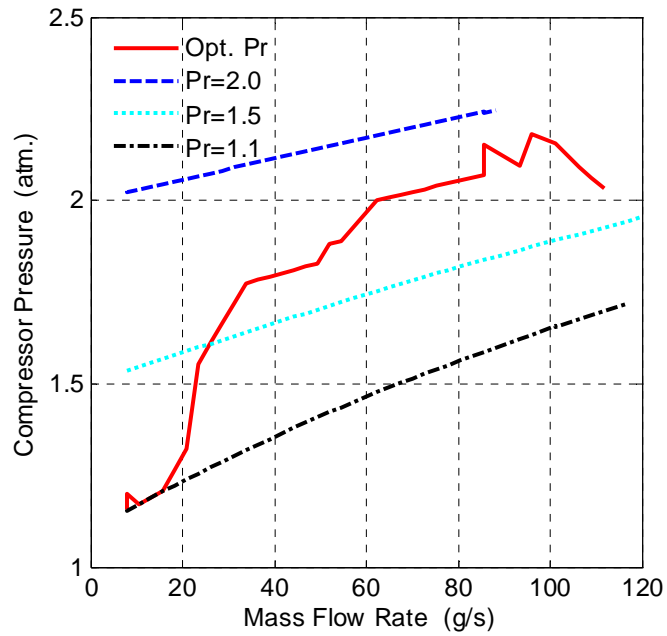
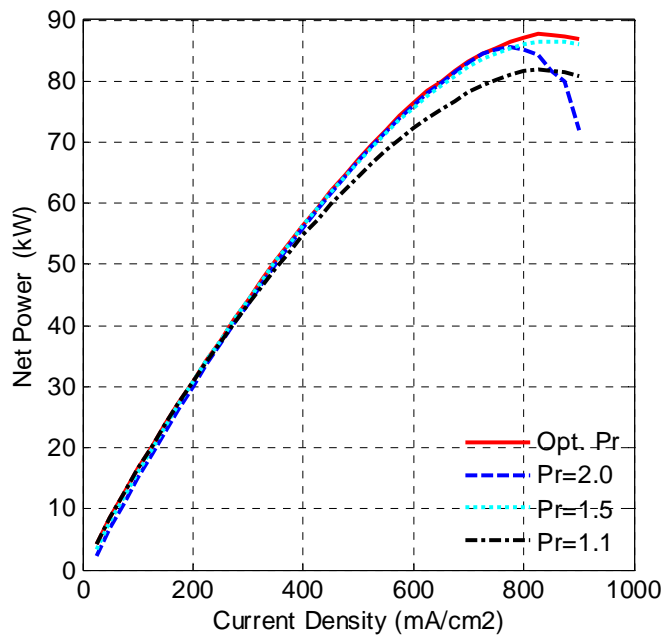
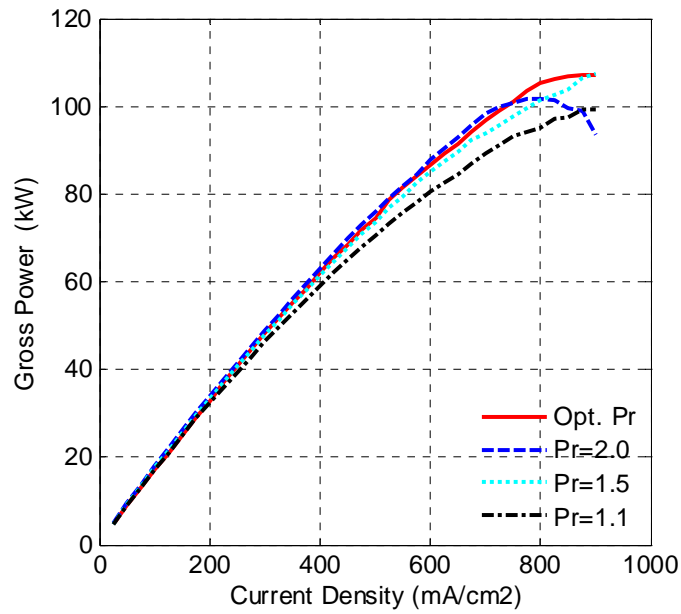


Figure 11 Compressor quasi-steady responses for different operating modes



**Figure 12 Fuel cell system net power vs. current density**



**Figure 13 Stack gross power vs. current density**

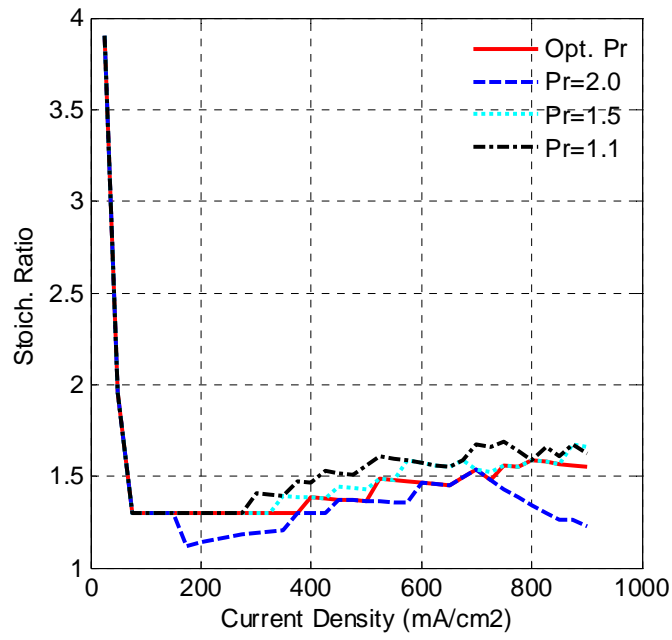


Figure 14 Air supply stoich. ratio vs. current density

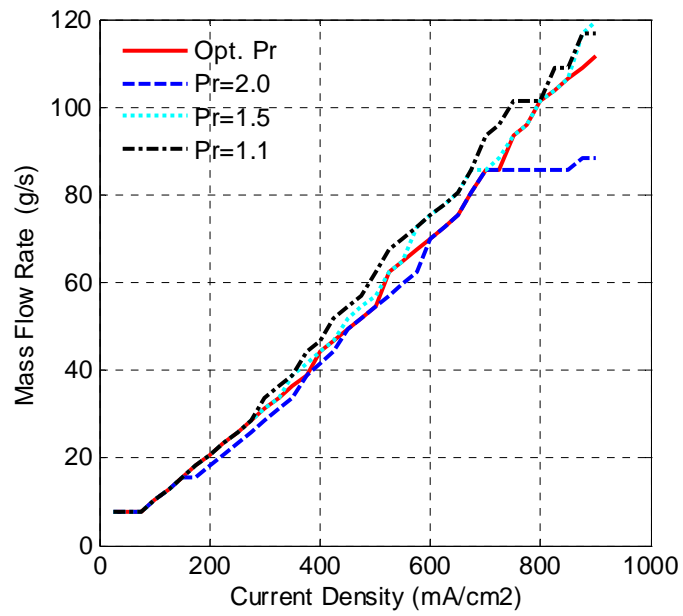


Figure 15 Dry air mass flow vs. current density

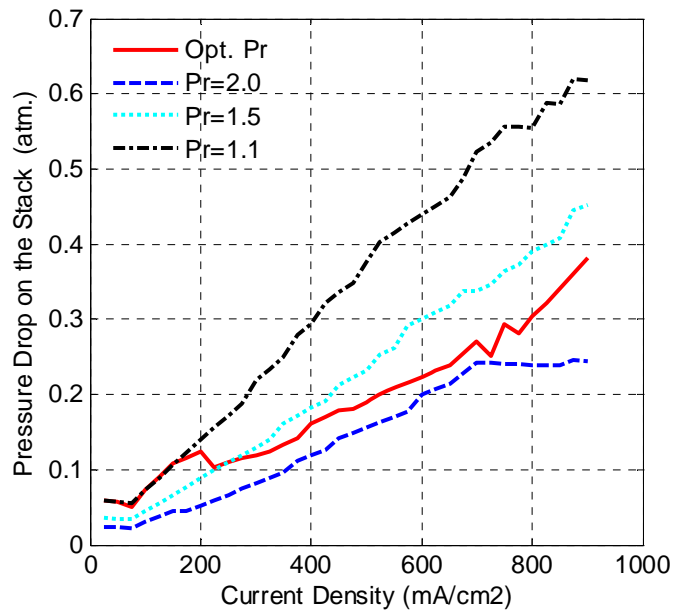


Figure 16 Pressure drop across the stack vs. current density

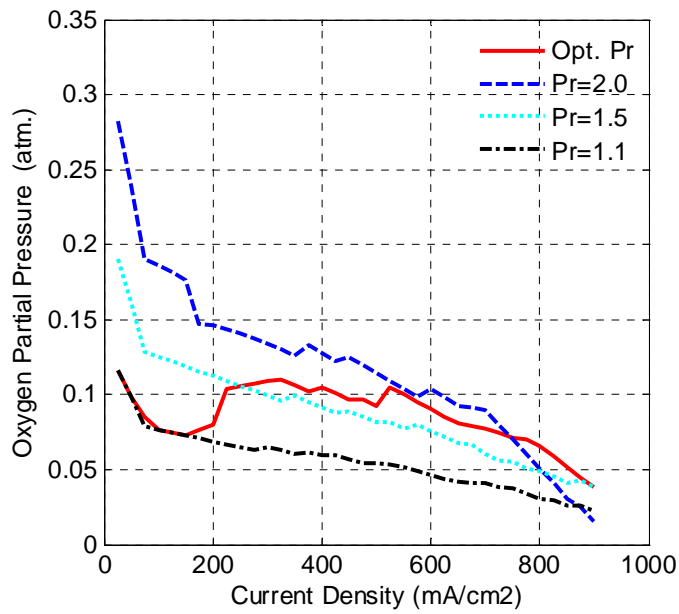


Figure 17 Oxygen partial pressure at the catalyst layer vs. current density

The comparisons indicate that each operating mode has its advantages and disadvantages.

- The fuel cell system with optimal varying back pressure can achieve higher system efficiency over the full load range (Figure 9) and can produce more power than the fuel cell system operating at constant back pressure (Figure 12).
- For the same fuel cell system with different operating modes, lower constant back pressure operation has higher pressure drop across the stack than other operating modes due to higher ratio of water vapor partial pressure and dry air partial pressure, as shown in Figure 16.
- At low power demand, the fuel cell system operating at low pressure and at optimal back pressure has higher system efficiency than the fuel cell system operating at high pressure because of relatively low parasitic losses.
- At high power demand, the high pressure operating mode and the optimal varying back pressure operation mode can achieve higher system efficiency compared to low pressure operation due to the high oxygen partial pressure at the catalyst layer and low pressure loss on the stack.
- At medium load demand, there is no apparent difference in the system efficiency for different operation modes. However, in addition to system efficiency, the size of the system should also be considered for the automotive applications. For example, low pressure operation requires a larger humidifier than high pressure operation.
- The optimal operation can achieve higher efficiency over wide load change. However, coordinated control of the compressor and the back pressure valve is complicated and is needed to avoid unacceptable large transient voltage drops during rapid load change (detailed in the dynamic model).

## 4 Dynamic Modeling and Control

The transient behavior of the air supply system will affect the performance of the fuel cell system due to the relatively slow response of the compressor, manifold filling/emptying, and the pressure control valve. To understand the dynamics of the fuel cell system and its effect on the vehicle performance, a model that accounts for the response time of the compressor was developed. The spatial variation of temperature, humidity, pressure, and flow rate etc. in the air system components is approximated or averaged. A filling/emptying model approach similar to papers [15,18] was used to avoid linearization of the air supply system around the set points. The variables to be controlled are the air mass flow through the cathode and the stack back pressure. A twin screw compressor is employed to control the mass flow and a pressure valve is used to control the back pressure of the stack. Conventional feed forward and feedback control are employed to control the mass flow and back pressure around the optimum operating conditions which were generated from the quasi-steady fuel cell system optimization model. The varying pressure loss across the stack due to flow friction is included by using the Darcy-Weisbach law. The fuel cell stack model [5] derived from a basic diagnostic fuel cell model [3] was used to predict the stack voltage for various operating conditions such as stack current, temperature, back pressure, and mass flow.

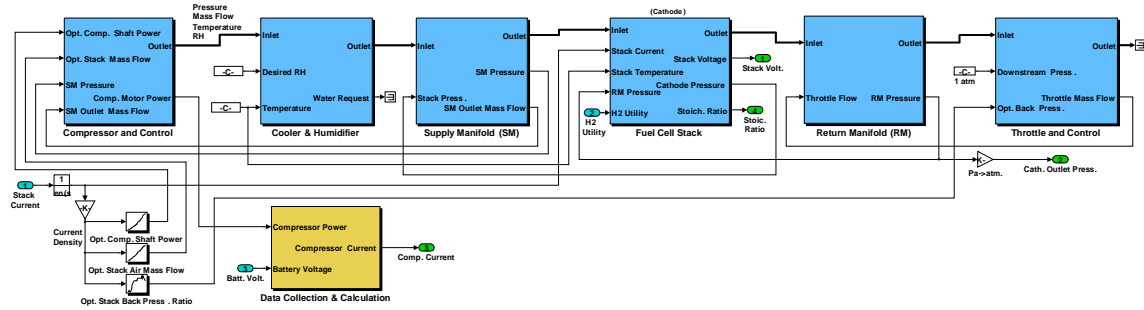


**Figure 18 Diagram of the dynamic fuel cell system model (Air supply)**

The dynamic air supply system model consists of the compressor and control, supply manifold, cooler and humidifier, fuel cell stack, return manifold, and throttle and control. To ensure that each of the components in the model is realistically represented, the model incorporates either fundamental models, as in the fuel cell stack, or performance based maps, as for the compressor. The model was developed by using Matlab®/Simulink®, as shown in Figure 18. The inputs are the required current and the optimum operating conditions for the system and the output is the stack voltage.

#### **4.1 Dynamic Compressor Model and Control**

The state of the compressor is tracked in terms of its rotational speed, which is strongly dependent on its inertia during transients. The compressor is sized using the factor  $k$  as previously discussed. The performance of the compressor is determined from the scaled maps of a Vairex twin screw compressor, which gives compressor speed, power, and air temperature as functions of pressure and air mass flow.

The speed of the compressor can be calculated from

$$J_{cp} \frac{dw_{cp}}{dt} = T_{em} - T_{cp} = \frac{1}{w_{cp}} (P_{em} - P_{cp}) \quad (11)$$

where  $J_{cp}$  is the combined inertia of the compressor and the motor corrected by their gear ratio,  $w_{cp}$  is the rotary speed of the compressor;  $T_{em}$ ,  $P_{em}$ ,  $T_{cp}$  and  $P_{cp}$ , respectively, denote the electromagnetic torque and power of the motor and the required torque and power from the compressor. The speed and torque of the motor are constrained by its specifications. The efficiency of the motor is determined from a scaled power/speed map of a Solectria induction motor.

The block diagram for calculating the compressor rotary speed is shown in Figure 19. The compressor speed is calculated by a lumped rotational inertia model utilizing the difference in the power/torque required to drive the compressor and the applied motor shaft power/torque. The corrected inertia based on the reduction gear ratio between the compressor and motor is used in the equation (11).

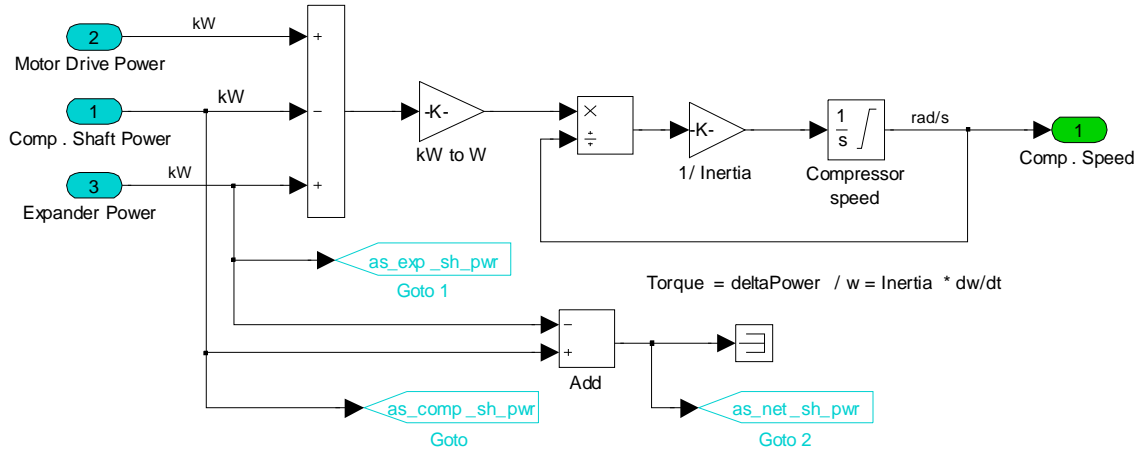


**Figure 19 Compressor speed calculation**

The operating point of the compressor depends on its speed and the stack back pressure and mass flow. The basic objective of the compressor control is to regulate the mass flow to meet the optimal mass flow for each stack condition. Compared with the fuel supply loop, the air supply has a poor dynamic response that makes control a difficult task and can introduce significant efficiency losses. The control is accomplished through a combination of a conventional feed forward and feedback control, as shown in Figure 20. The static feed forward component is simply implemented with a look-up table – an optimal compressor shaft power indexed by the current density. A closed-loop model relating the optimal air mass flow to the actual air mass flow and a PI controller are implemented to improve the system robustness. The feed forward and feedback components are summed as the required compressor motor drive power.

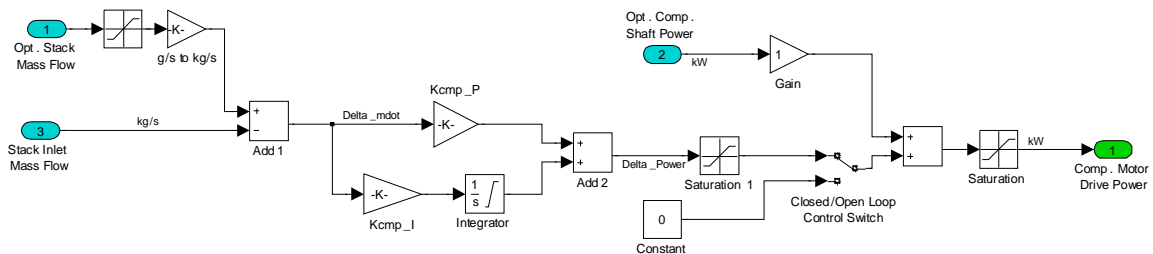


**Figure 20 Diagram of compressor drive motor control**

The air compressor is modeled with maps. These maps relate the pressure and mass flow to the compressor shaft power, compressor speed, and air output temperature. An air screw compressor is used in this model. The compressor shaft power is obtained through a lookup table from the compressor downstream pressure and mass flow. An efficiency

map for the combination of a motor and controller is used to obtain the power request of the compressor drive motor as shown in Figure 21. Since the compressor speed map is not suited for obtaining the air mass flow from the compressor speed and pressure, a two-layer 20-neuron neural network trained with the reshaped data from the compressor speed map is used to reconstitute the compressor map for the calculation of the air mass flow from the compressor shaft speed and back pressure as shown in Figure 22. The input  $p\{1\}$  is the downstream pressure and shaft speed, the output  $y\{1\}$ , the air mass flow.

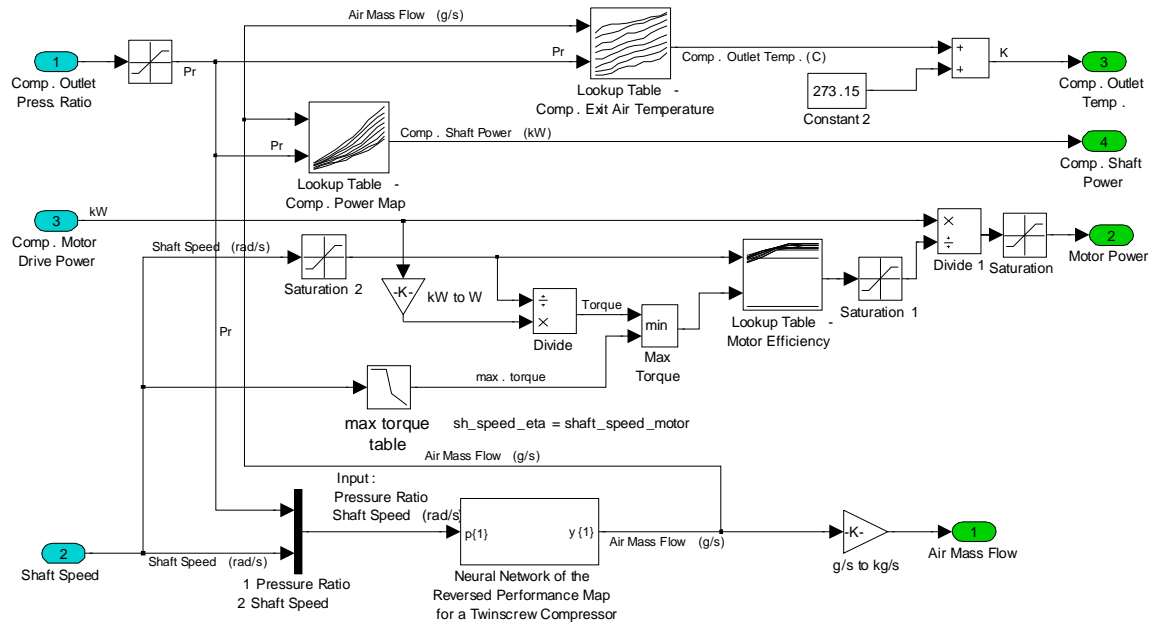


Figure 21 Diagram of compressor and drive motor performance

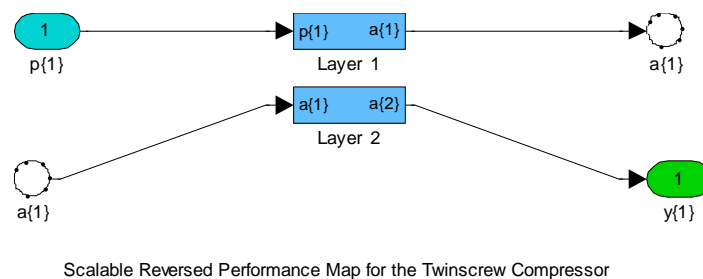


Figure 22 Neural net work for the mass flow rate calculation

## 4.2 Lumped Manifold/Cathode Model

The spatial dependence of variables such as temperature, humidity, pressure, and flow rate has little effect on the behavior of the fuel cell system. Hence these variables are approximated or averaged in the model and lumped as a function of time alone

throughout the lump volume. Furthermore, it is assumed all gases behave as an ideal gas and excess water vapor condenses into a liquid form. The equations for the lumped variables are derived from the conservation equations. The mass balance is expressed as

$$\frac{dm}{dt} = \dot{m}_{in} - \dot{m}_{out} \quad (12)$$

And the energy equation is given by

$$\frac{dp}{dt} = \frac{R}{V} (\dot{m}_{in} T_{in} - \dot{m}_{out} T_{out}) \quad (13)$$

where,  $m$  is the mass of humid air in the manifold,  $\dot{m}$  the mass flow,  $T$  the temperature,  $p$  the pressure in the manifold,  $R$  the gas coefficient of the humid air and  $V$  the lumped volume of the manifold. The subscripts *in* and *out* denote the inlet flow and the outlet flow, respectively.  $R$  is obtained using the molecular weight of the humid air which varies slightly with the pressure and temperature.

The flow friction drop in the supply and return manifolds are neglected compared to that in the channels of the fuel cell stack. Therefore, only the pressure loss across the stack is considered. The pressure drop across the stack can be divided into two parts: the pressure loss in the vertical inlet/outlet manifold and the pressure drop in the flow paths in the flow field plates. Usually, the pressure drop in the inlet/outlet manifold is less than a quarter of the pressure drop across the flow field plates. The flow in the channels of the fuel cell plates is considered laminar depending on the flow velocity and the flow field plate geometry. It is assumed that the flow in the channels is fully developed, steady, and incompressible. Applying the Darcy-Weisbach equation, the pressure drop is expressed as

$$\Delta P = \lambda \frac{L \rho v^2}{2 D_h} \quad (14)$$

where  $\lambda$  is the friction coefficient,  $\rho$  is the humid air density which is a function of pressure, humidity, and temperature,  $v$  is the flow velocity, and  $L$  and  $D_h$  are the equivalent length and hydraulic diameter of the channels, respectively.

For fully developed laminar flow, the roughness can be neglected. The friction coefficient as a function of Reynolds number can be expressed as:

$$\lambda = \frac{64}{R_e} = \frac{64 \mu}{D_h v \rho} \quad (15)$$

where  $R_e$  is the Reynolds number, and  $\mu$  is the dynamic or absolute viscosity. Substituting equation (15) into (14) yields the relationship between pressure drop and mass flow rate in the flow channel

$$\dot{m}_{ch} = \frac{\rho A_{ch} D_h^2}{32 \mu L k} \Delta P \quad (16)$$

where  $A_{ch}$  is the cross section area of the flow channel, and  $k$  is the correction coefficient for the pressure loss on the vertical inlet/outlet manifold.

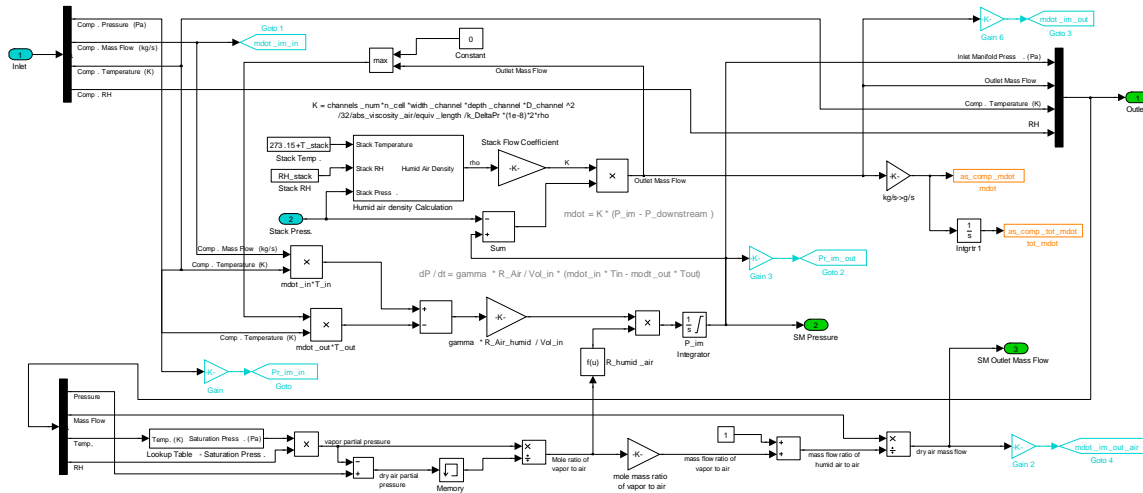


Figure 23 Block diagram of the supply manifold

The diagram of the supply manifold block is given in Figure 23. The inlet and outlet mass flows determine the pressure in the supply manifold from equation (12) and (13). The outlet mass flow rate can be obtained from the supply manifold pressure and the downstream pressure from equation (16). For the cathode side of the stack, since part of oxygen will be consumed due to the electrochemical reaction, the mass and energy balance are complicated. The principles of mass and the energy conservation are applied to the oxygen, nitrogen, and water vapor flows. The pressure in the cathode can be obtained by adding the partial pressure of each of the species. The volume of the supply and return manifolds is fixed and the volume of the cathode channel area can be calculated from the channel dimensions and channel number.

### 4.3 Cooling/Humidifier and Throttle Control

It is assumed that the cooling loop and the humidifier are well controlled at the set points and the pressure inside the humidifier will not change and the increase of the vapor partial pressure is equal to the decrease of the dry air partial pressure. Hence

$$P_{inlet} = P_{outlet} \quad (17)$$

$$\Delta p_{dry\ air} = \Delta p_{vapor} \quad (18)$$

The principle of mass conservation is used to calculate the outlet mass flow rate of the humidifier.

$$\dot{m}_{humid\ air} = \dot{m}_{dry\ air} + \dot{m}_{vapor} \quad (19)$$

Figure 24 gives the diagram of the cooler and humidifier block. The water vapor partial pressure is obtained from a lookup table indexed by temperature and the set relative humidification. The required water injection is calculated from the mole ratio of the water vapor and the dry air.

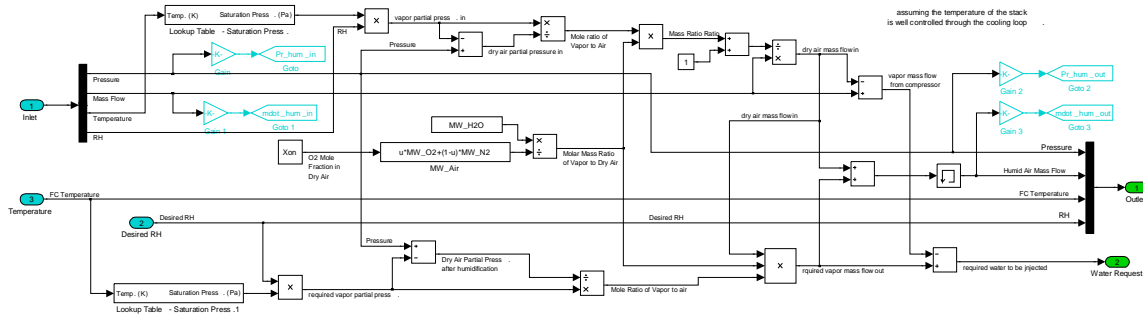


Figure 24 Block diagram of the Cooler and Humidifier

A back pressure valve is used for regulating the back pressure. The nozzle equation from [23] is employed to model the relationship between the pressure drop and the outlet flow.

$$\dot{m} = \begin{cases} \frac{C_D A_T p}{\sqrt{RT}} \gamma^{1/2} \left( \frac{2}{\gamma+1} \right)^{\frac{\gamma+1}{\gamma-1}} \text{ If } \frac{p_0}{p} \leq \left( \frac{2}{\gamma+1} \right)^{\frac{\gamma}{\gamma-1}} \\ \frac{C_D A_T p}{\sqrt{RT}} \left( \frac{p_0}{p} \right)^{\frac{1}{\gamma}} \left\{ \frac{2\gamma}{\gamma-1} \left[ 1 - \left( \frac{p_0}{p} \right)^{\frac{\gamma-1}{\gamma}} \right] \right\}^{1/2} \text{ others} \end{cases} \quad (20)$$

where  $C_D$  is the discharge coefficient,  $p_0$  is the down stream pressure of the nozzle, and  $\gamma = 1.4$  for air.  $A_T$  is the opening area of the nozzle.

The back pressure control is accomplished by adjusting the effective opening area of the valve through a combination of a conventional feed forward and feedback control as shown in Figure 25. The static feed forward component of the effective opening area is simply calculated with the nozzle equation (20) according to the optimal back pressure. The feedback component is obtained through a feedback PI control relating the optimal

back pressure to the actual back pressure. The feed forward and feedback components are summed as the effective opening area demand.

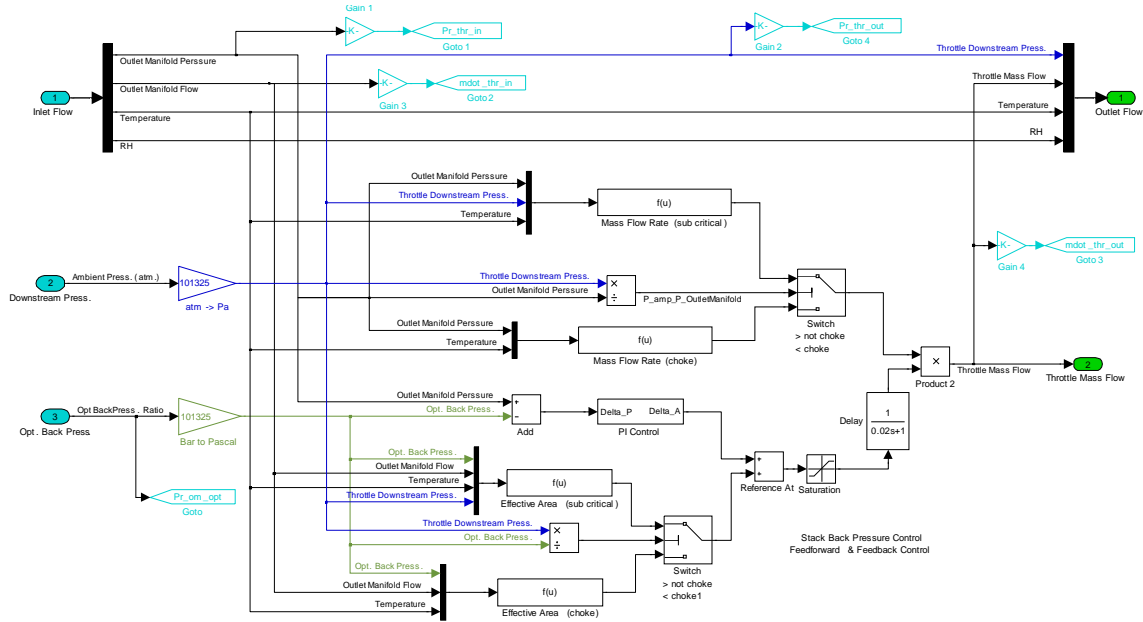


Figure 25 Diagram of the back pressure throttle and control

## 4.4 Fuel Cell Model

The electrochemical reactions are very rapid making the response time of the cells very short (milliseconds). Therefore, the quasi-steady fuel cell model ( $V_{cell}$  vs.  $J$ ,  $P$ , SR in the cells) developed in the FCVMP program [5] is employed in this dynamic model. Other fuel cell models could be utilized if available. The single cell model used was developed from Springer's single diagnostic cell model [3]. The fundamental equation is

$$V_{cell} = V_o - I \cdot R - \eta_{anode} - \eta_{cathode} \quad (21)$$

where  $V_o$  is the reference voltage of 0.9 V,  $I$  the current density,  $R$  the internal membrane resistance.  $\eta_{anode}$ ,  $\eta_{cathode}$  denote the anode and cathode overpotentials, respectively. The oxygen partial pressure at the backing/catalyst layer interface is given by [3]

$$p_{ox} = p(1 - x_{ws}) \left[ 1 - (1 - x_{eff}) e^{I/I_B} \right] \quad (22)$$

where  $p$  is the total pressure,  $x_{ws}$  the water vapor mole fraction,  $x_{eff}$  the effective oxygen mole fraction,  $I_B$  the backing characteristic current density. The Simulink block models for calculating the oxygen partial pressure and for predicting the cell voltage are shown in Figure 26 and Figure 27.

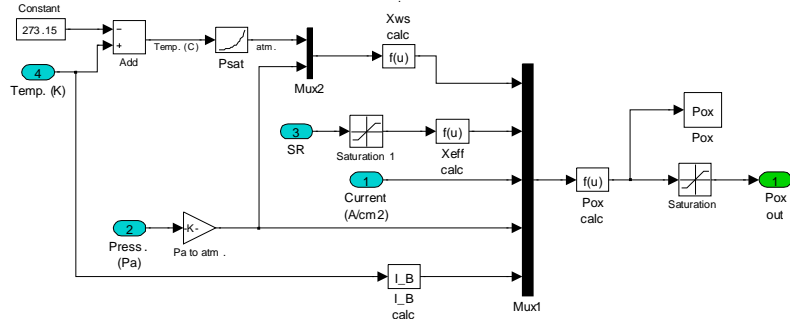


Figure 26 Diagram for the oxygen partial pressure calculation

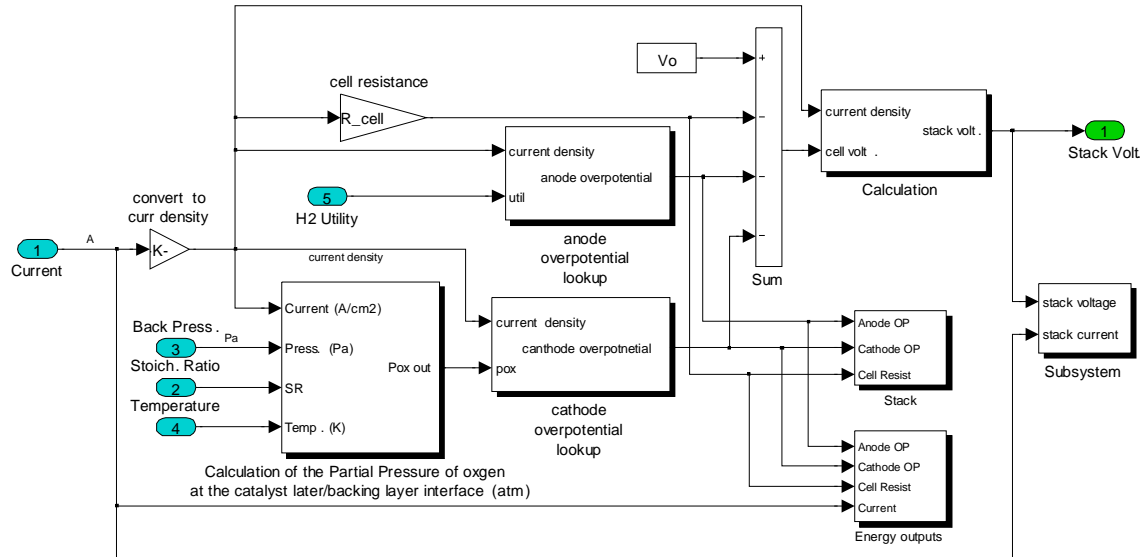


Figure 27 Block diagram of the fuel cell model

## 5 Fuel Cell System and Vehicle Simulation Results

### 5.1 Results for the Dynamic Fuel Cell System

The dynamic model for the stand-alone fuel cell system was run for a series of current steps. The key fuel cell parameters are given in Table 2. The back pressure and air mass flow were controlled around the optimum operating conditions. As shown in Figure 28, good transient response and control were achieved for the complete range of currents (up to 300A) using the conventional feed forward and feed back control. The system power flow and efficiency are shown in Figure 29. The results indicate that the transient effects of the compressor dynamics and manifold filling/emptying have a large impact on the output voltage of the stack and introduce an efficiency loss at the times of step current changes. Air starvation can occur when the system is operating in low pressure condition. The transient response of the compressor and the simulation result from the quasi-steady system optimization model are presented in Figure 30. The transient polarization curve of the fuel cell under the step current is shown in Figure 31. The pressures in the supply

manifold, fuel cell cathode side, and the return manifold are plotted in Figure 32. Figure 33 presents the change of the mass flow after humidification. The outlet mass flow of the compressor and the inlet mass flow of the stack are plotted. The response of the system with and without the closed-loop mass flow control is given in Figure 34. It can be seen that a closed-loop mass flow control can improve the response time and the system robustness.

**Table 2 Fuel cell system parameters (case 1)**

Fuel Cell System Parameters	
Supply Manifold Volume (m <sup>3</sup> )	0.02
Return Manifold Volume (m <sup>3</sup> )	0.003
Calculated Cathode Channel Volume (m <sup>3</sup> )	0.009
Combined Compressor Inertia (kg*m <sup>2</sup> )	0.0124
Compressor Gear Ratio	2.84

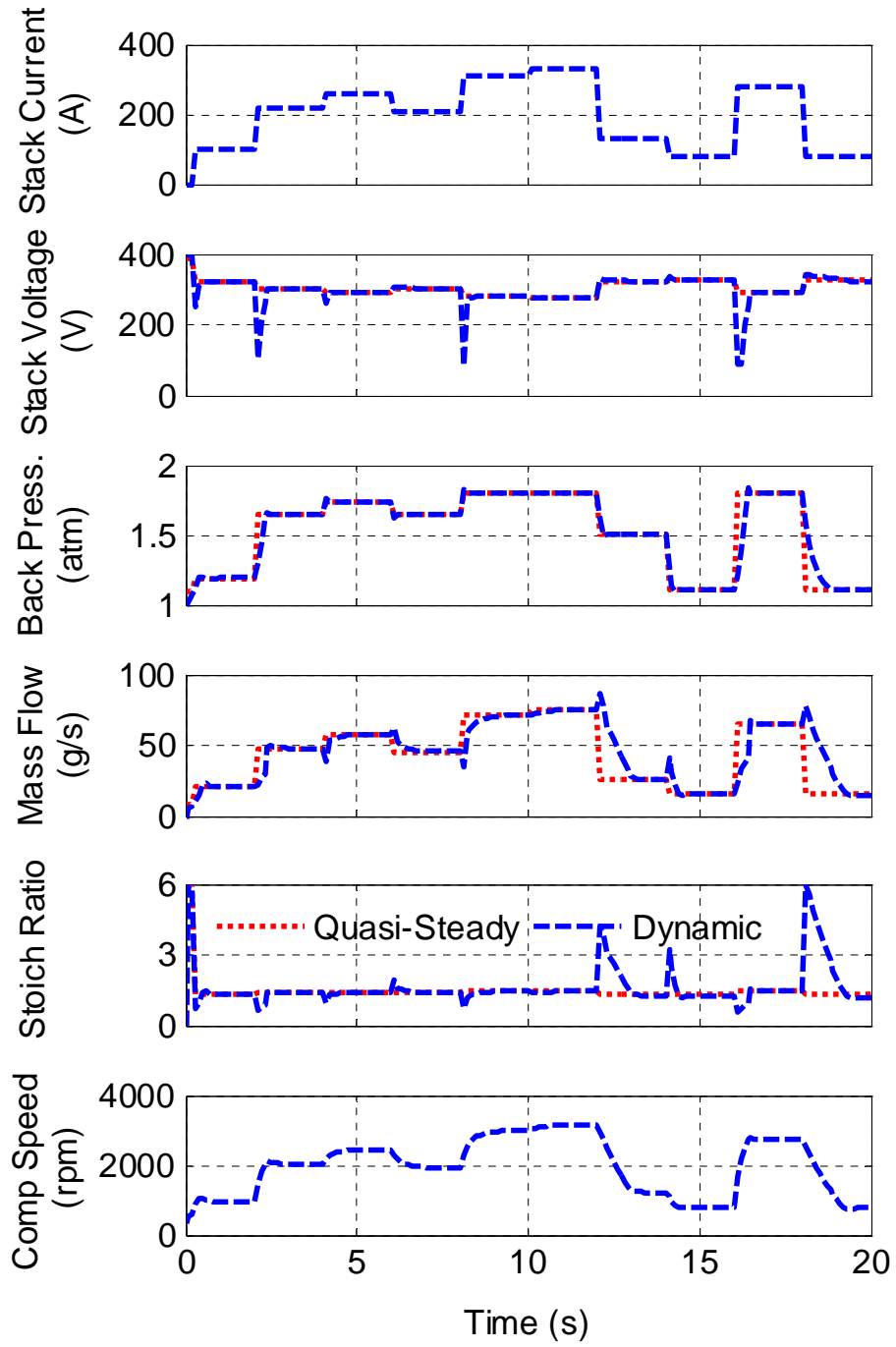


Figure 28 Transient response of the fuel cell system under a series of step current

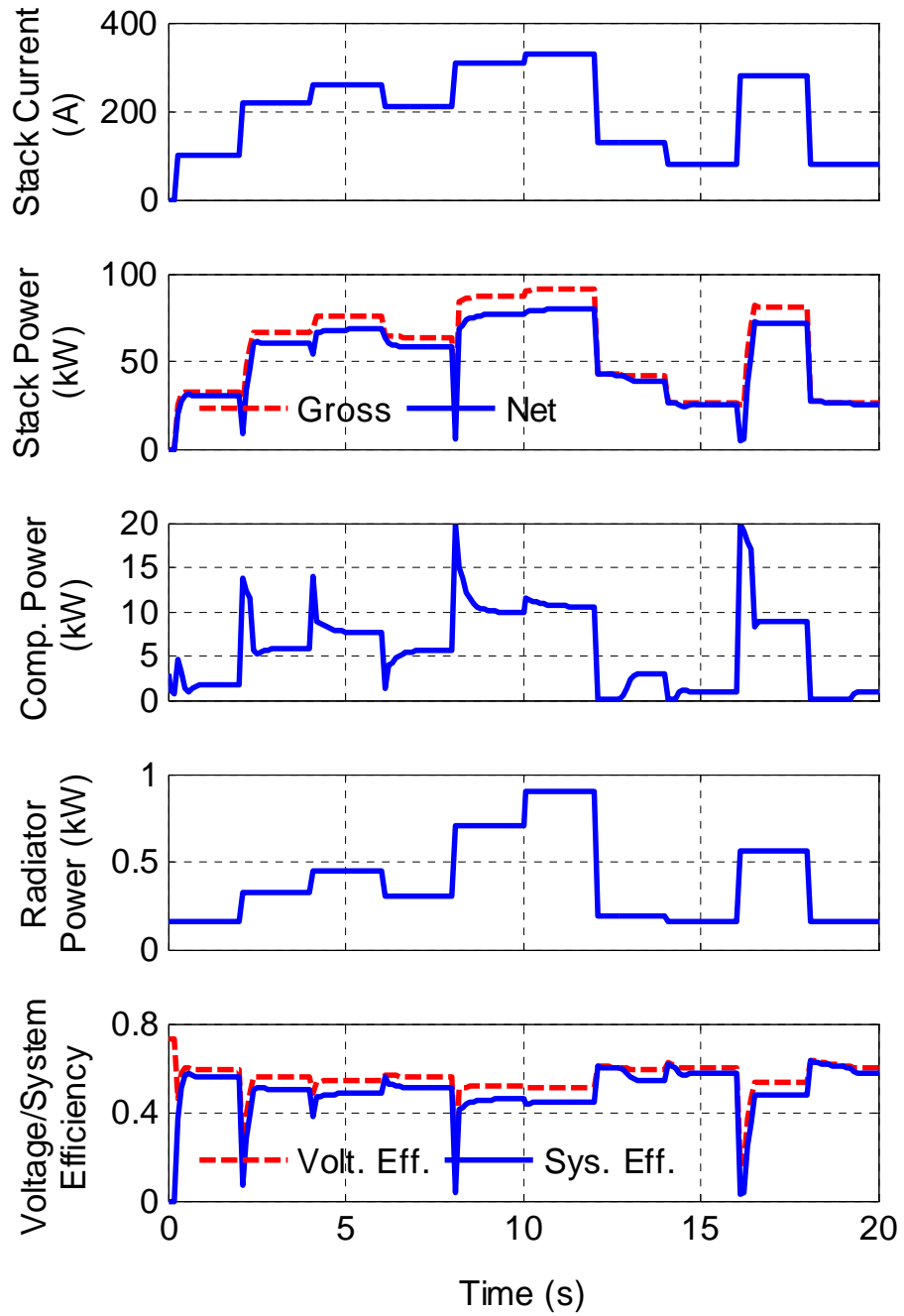
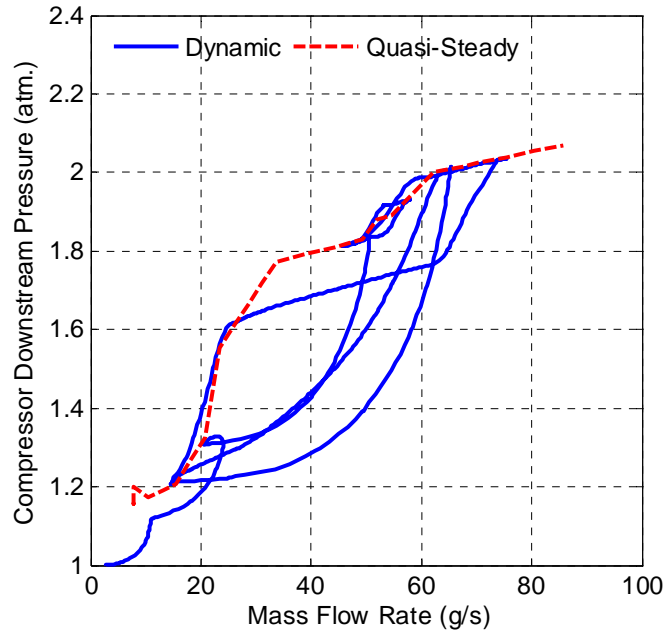
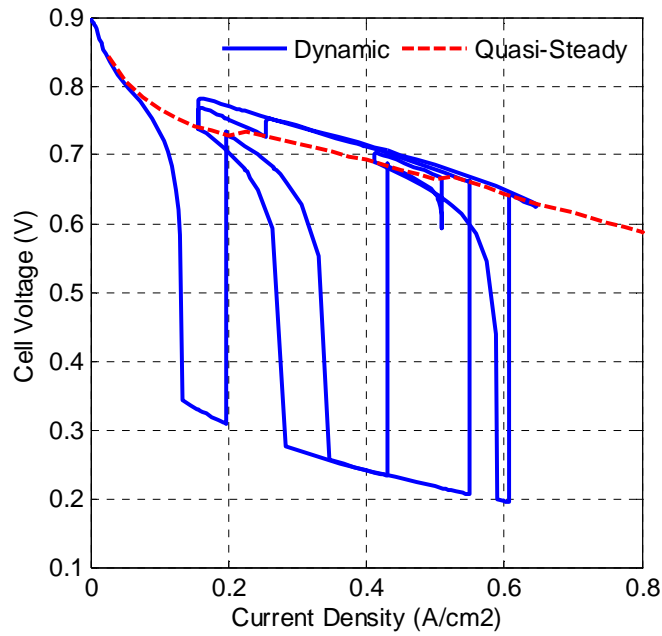


Figure 29 Simulation results of system power flow and efficiency



**Figure 30 Performance control response of the compressor**



**Figure 31 Comparison of current-voltage trajectory from the dynamic model and the quasi-steady optimization model**

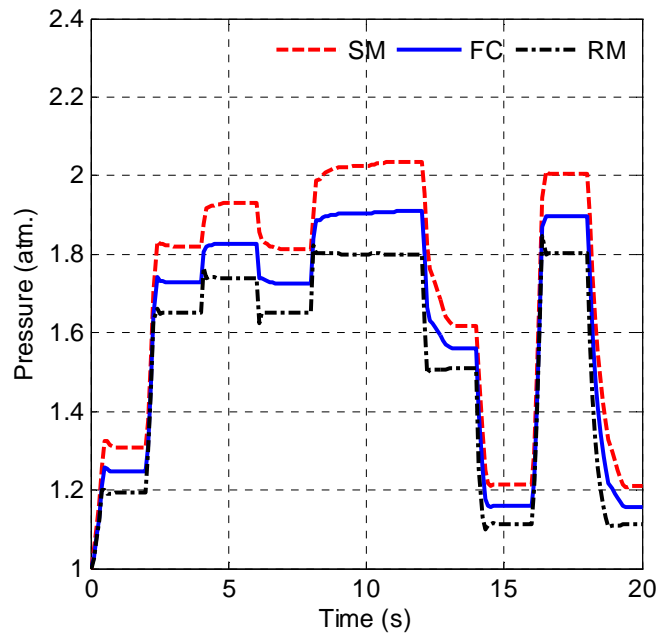


**Figure 32** Pressure responses of the supply manifold, fuel cell cathode, and the return manifold (SM, FC, and RM denote the supply manifold, Fuel cell cathode side, and the return manifold, respectively)

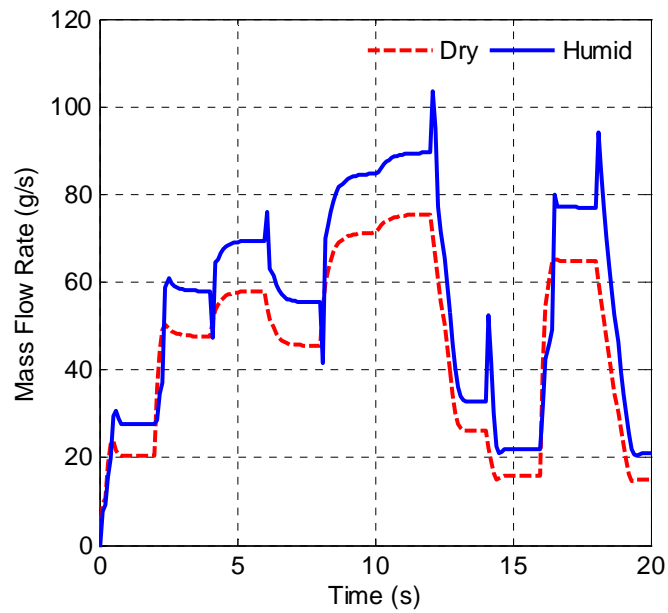


**Figure 33** Mass flow trajectory of the compressor outlet flow (dry air) and the fuel cell inlet flow (fully humidified air) under the step current

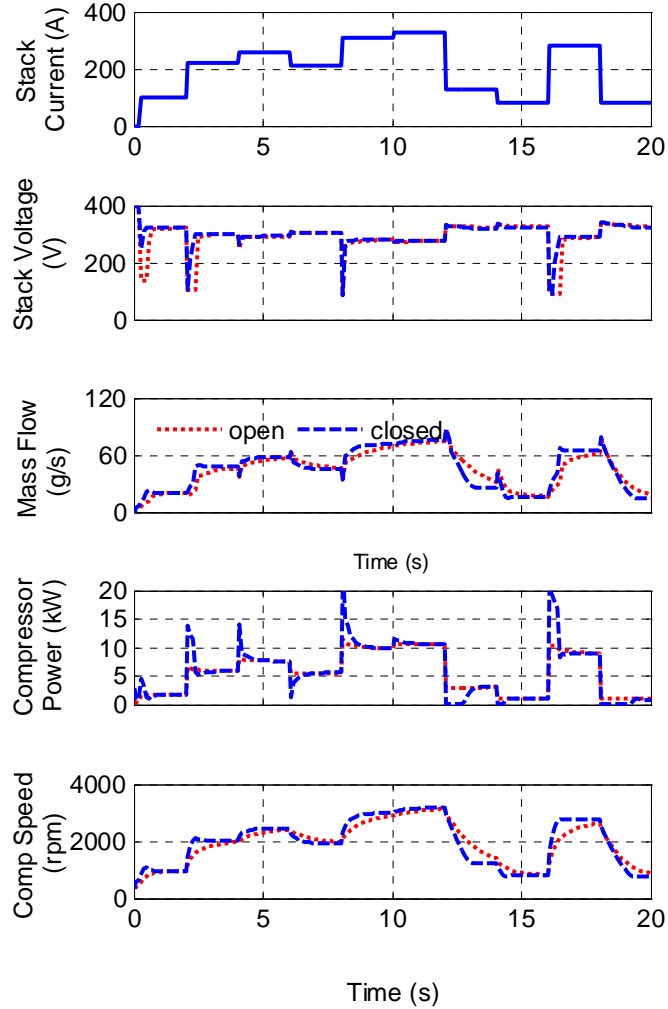


**Figure 34 Comparison of the transient response of the system with a closed-loop control of the mass flow rate and without a feedback mass flow control (feed forward control only)**

## **5.2 Simulation Results of Fuel Cell Vehicles**

The dynamic fuel cell system model was integrated into a forward-looking vehicle model of a load-following direct hydrogen fuel cell vehicle (DHFC) [8]. Compared to the original UC Davis fuel cell model [22, 24], the present DHFC model employs an updated traction motor controller (details in the Appendix 4) and the scalable dynamic fuel cell system model that allows simulations of not only vehicle dynamics but also fuel cell system transient response. Simulations were performed for FUDS drive cycle with the quasi-steady and dynamic fuel cell system models. The simulation results given in Figure 35 and 36 show that the vehicle can follow the driving cycle without difficulty using both the quasi-steady and transient dynamic fuel cell system models. However, the vehicle model with the dynamic fuel cell system has larger voltage fluctuations as would be expected. The large voltage drops occur during fast acceleration. These large

voltages drops would no be acceptable in practice and should be eliminated. One approach to doing that is to utilize a battery or ultracapacitor as energy storage to load level the fuel cell operation. Figure 37 shows the efficiencies of the fuel cell system on the FUDS cycle for the quasi-steady and dynamic fuel cell models. It can be seen that the maximum power required during the FUDS drive cycle was approximated 40 kW. Most of the time the fuel cell operates in the low power range. The differences in the efficiencies are not large except at high power where the dynamic model shows large and erratic changes.

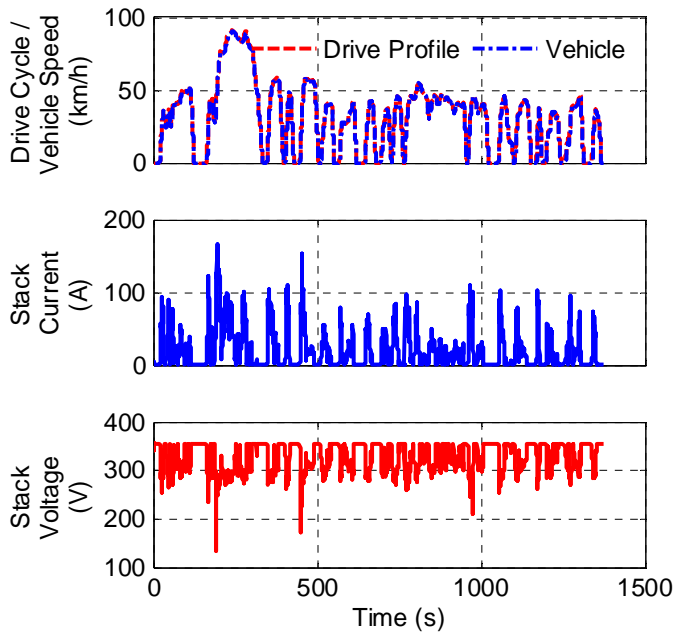


**Figure 35 Simulation results of the DHFC vehicle with the dynamic fuel cell system model on the FUDS cycle**

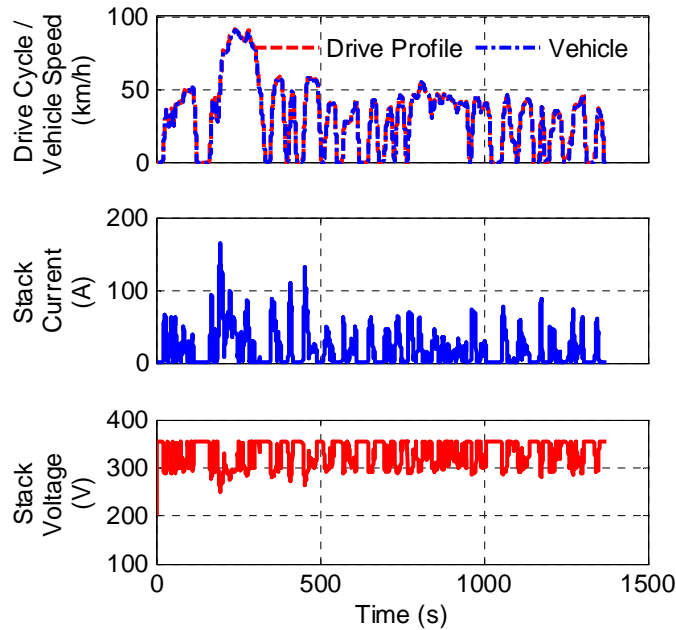


**Figure 36 Simulation results of the DHFC vehicle with quasi-steady state fuel cell system model on the FUDS cycle**

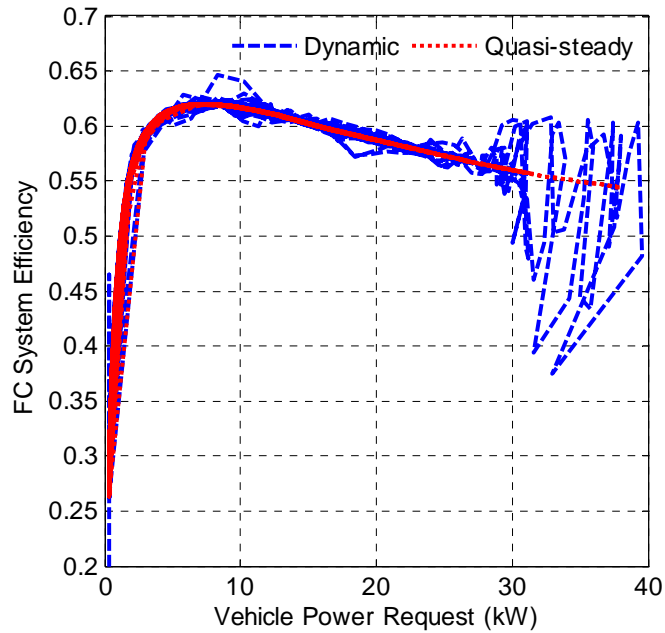


**Figure 37 Comparison of the system performance with the quasi-steady and dynamic fuel cell system model on FUDS drive cycle**

The effect of the dynamics of the fuel cell system on the vehicle fuel economy on various drive cycles was also studied. The key vehicle and fuel cell system parameters used for the simulations are shown in Table 3 (Case 1). The fuel economies for the various driving cycles are shown in Figure 38. The results indicate that including the transient dynamics when the fuel cell system is operated at optimal conditions has no apparent effect on fuel

economy (less than 1 percent) compared to the quasi-steady mode. This is a surprising result.

**Table 3 Vehicle and fuel cell system parameters (Case 1)**

Vehicle and System Parameters	
Drag Coefficient	0.3
Frontal Area (m <sup>2</sup> )	2.2
Vehicle Hotel Load (kW)	0.3
Vehicle Mass (kg)	1500.0
Electric Motor (kW)	75.0
Fuel Cell Stack and Auxiliaries	
Max. Net Power (kW)	87.6
Gross Power (kW)	106.2
Number of Cells	440
Cell Area (cm <sup>2</sup> )	510.0
Compressor (kW)	17.2

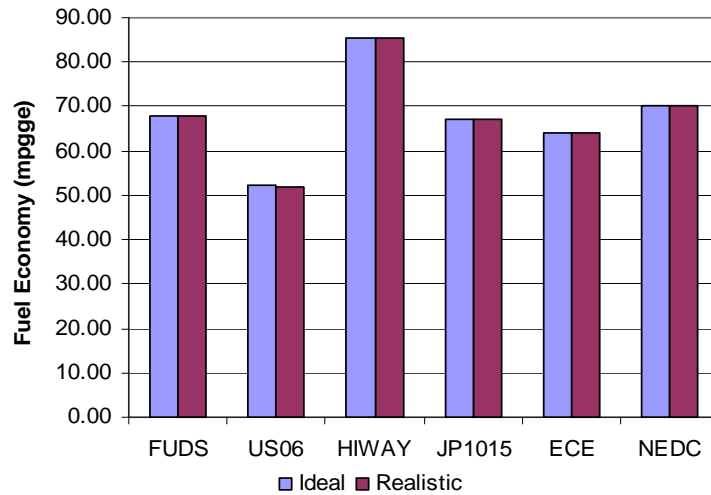


**Figure 38 Fuel economy (gasoline equivalent) of the DHFC vehicle with the quasi-steady state and with dynamic fuel cell system model on different driving cycles (Case 1)**

Simulations were also performed for the vehicle in Case 1 with the fuel cell system operating at constant back pressures of 2.0 atm., 1.5 atm. and 1.1 atm. and optimal SR. The fuel economies for the various driving cycles are shown in Figure 39. The results indicate that optimal operation, including varying the back pressure, can achieve a higher vehicle fuel economy compared to constant high back pressure operation. The vehicle with the fuel cell system operating at constant low pressure has almost the same fuel economy as that of the vehicle with optimal varying back pressure operation. However, the low constant back pressure operation has lower maximum net output power, which will affect the vehicle acceleration performance.

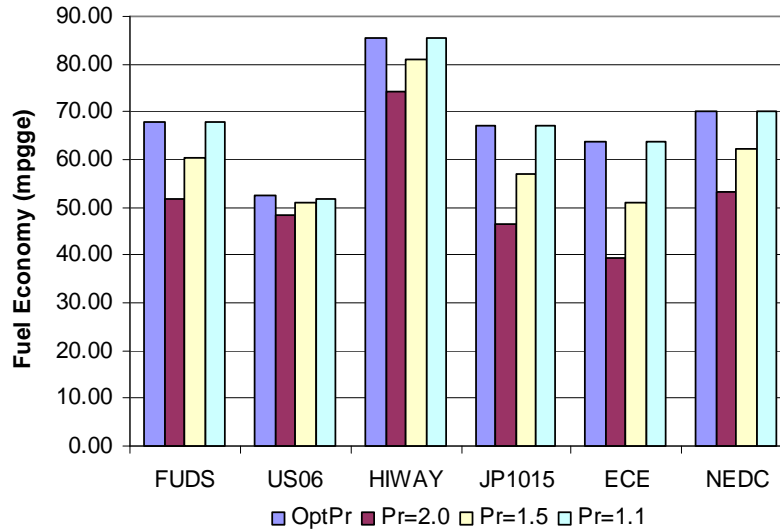


**Figure 39 Fuel economy of the DHFC vehicle operating at optimal back pressures and fixed back pressures of 2.0, 1.5, and 1.1 atm. on different driving cycles (Case 1)**

Additional simulations were performed with a smaller fuel cell system (Case 2) to address the effect of the size of the fuel cell system on the vehicle fuel economy. The vehicle and fuel cell system parameters are given in Table 4. The simulated vehicle fuel economies for the various driving cycles are presented in Figure 40. The vehicle fuel economy in Figure 40 was normalized with respect to corresponding fuel economy of Case 1 for the each drive cycle and plotted in Figure 41. It can be seen that employing a smaller fuel cell system in a DHFC vehicle has a little impact on the vehicle fuel economy for the optimal varying back pressure operation, but can significantly improve the fuel economy for the fixed high back pressure operation.

**Table 4 Vehicle and fuel cell system parameters (Case 2)**

Vehicle and System Parameters	
Drag Coefficient	0.3
Frontal Area (m <sup>2</sup> )	2.2
Vehicle Hotel Load (kW)	0.3
Vehicle Mass (kg)	1500.0
Electric Motor (kW)	50.0
Fuel Cell Stack and Auxiliaries	
Max. Net Power (kW)	58.4
Gross Power (kW)	70.8
Number of Cells	440
Cell Area (cm <sup>2</sup> )	340
Compressor (kW)	11.4

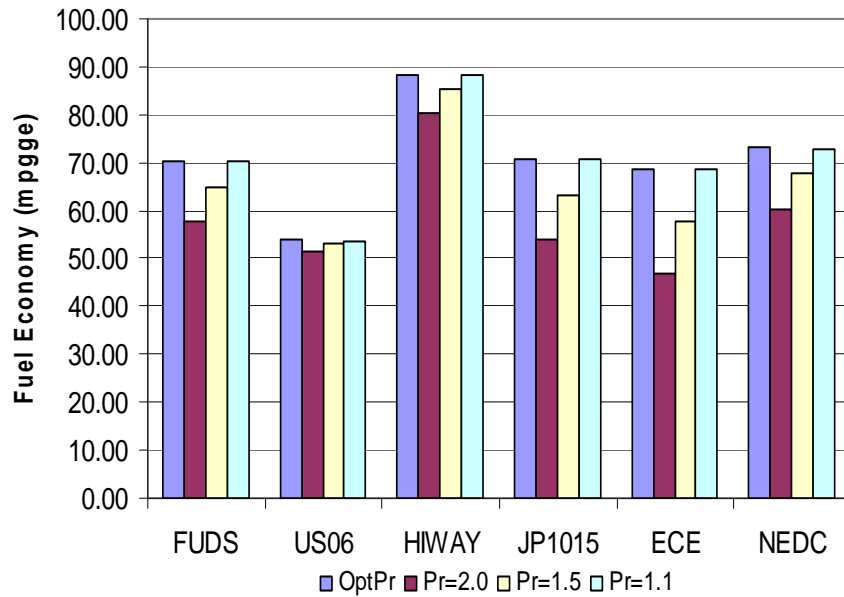


**Figure 40 Fuel economy of the DHFC vehicle with a smaller fuel cell system operating at optimal back pressures and fixed back pressures of 2.0, 1.5, and 1.1 atm. on different driving cycles (Case 2)**

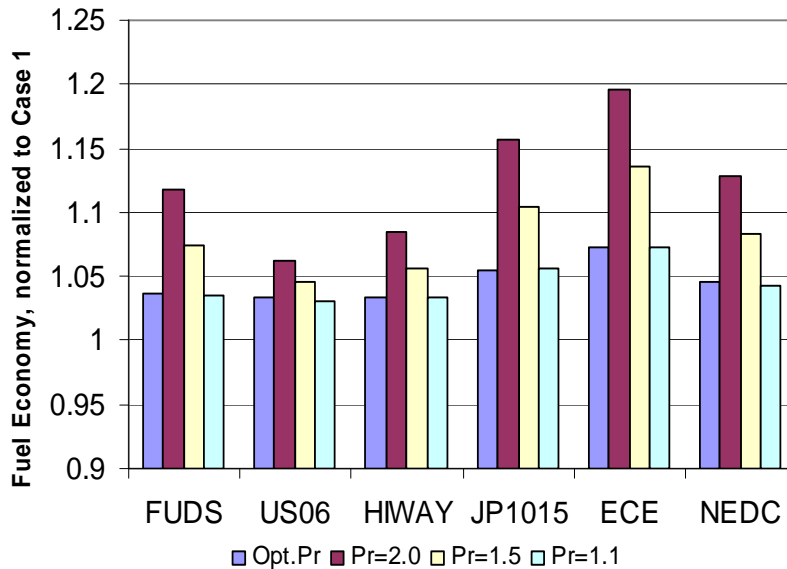


**Figure 41 Normalized fuel economy of the DHFC vehicle (case 2: a small fuel cell system) to the DHFC vehicle (case 1)**

## 6 Conclusions and Discussion

A scalable fuel cell system optimization model was developed for determining the design parameters and optimum operating conditions for vehicle applications. The design parameters of the stack and sizing of the air supply and the water and thermal

management subsystems were taken into account with the objective of maximizing the system efficiency. A scalable dynamic model of the air supply system consisting of the compressor, lumped filling/emptying manifold and cathode side, and the back pressure throttle was developed. The dynamic fuel cell system model shows good transient response and can be controlled around the optimum operating conditions through a conventional feed forward and feedback control. The dynamic model of the fuel cell system was integrated in to a load-following fuel cell vehicle model. Vehicle simulations were performed for various driving cycles to study the effect of the system dynamics on vehicle fuel economy for the different size (kW) fuel cell systems..

The results of the study are summarized below:

- Compared to the constant back pressure operation, the fuel cell system with the optimal varying back pressure operation can achieve higher system efficiency over the operating power range and maximize the net system power.
- The dynamics of the fuel cell system introduce significant voltage drops during sudden changes in power demand due to air starvation when the load current increases sharply, especially for the fuel cell system operating in the low pressure region.
- The vehicle fuel economy results obtained using an optimal, dynamic model for the fuel cell system were nearly the same as those obtained using an optimal, quasi-steady model of fuel cell operation.
- The vehicle simulation results did indicate a significant improvement in fuel economy for variable back pressure compared to fixed back pressure operation.
- For optimal fuel cell operation, the size (kW) of the fuel cell system has a little effect on the fuel economy of the vehicle for the various driving cycles simulated. . However, reducing the size of the fuel cell system will benefit the fuel economy for a fuel cell system operating at the fixed high back pressure, especially high pressure (2 atm.).

The optimal operation of a fuel cell system requires varying the back pressure and air supply SR according to the change of the power demand. These rapid changes in the operating conditions of the fuel cell stack can have a major impact on the lifetime of the fuel cell stack due to the mechanical stresses on the MEA and the stack accessory components. Coordinated control of the mass flow and pressure of the cathode and anode sides of the stack is also required. This is the main drawback of the optimal operation of the fuel cell system for automotive applications. These variations in operating conditions can be reduced by hybridizing the fuel cell system by the addition of electrical energy storage with batteries or ultracapacitors. In addition to reducing the sudden changes in operating conditions, the energy storage permits the capture of regenerative braking energy, which will improve the fuel economy by 10-15%. The fuel cell – battery hybrid vehicle and its control strategy and the effect of the transient response of the fuel cell system on the hybridization will be addressed in the future work.

## Acknowledgements

The work presented in this report was supported by the STEPS and PHEV programs of the Institute of Transportation Studies of the University of California, Davis. This research benefited greatly from prior work performed by the UC Davis FCVMP team. Please refer to <http://www.its.ucdavis.edu> for further details about the STEP and PHEV programs, sponsors, and former works.

## References

1. R.K. Ahluwalia, X. Wang, R. Kumar, Fuel Cell Systems for Transportation: Status and Trends, *J. Power Sources*, 177(1), 2008, pp.167-176
2. T.E. Springer, T. A. Zawodzinski, S. Gottesfeld, Polymer Electrolyte Fuel Cell Model, *J. Electrochem. Soc.*, 138(8), 1991, pp. 2334-2342
3. T.E. Springer, M. S. Wilson, S. Gottesfeld, Modeling and Experimental Diagnostics in Polymer Electrolyte Fuel Cells, *J. Electrochem. Soc.*, 140(12), 1993, pp. 3513-352.
4. D.M. Bernardi, M.W. Verbrugge, A Mathematical Model of the Solid-Polymer-Electrolyte Fuel Cell, *J. Electrochem. Soc.*, 139(9), 1992, pp. 2477-2491.
5. D.J. Friedman and R.M. Moore, PEM Fuel Cell System Optimization, Proceedings of the 2<sup>nd</sup> International Symposium on Proton Conducting Membrane Fuel Cells II, Electrochemical Society, Pennington, NJ, 1998, p. 407-423.
6. P. Badrinarayanan, A. Eggert, R.M. Moore, Minimizing the Water and Thermal Management Parasitic Loads in Fuel Cell Vehicles, *International Journal of Transport Phenomena*, 2001 3(3) 213-229.
7. J.M. Cunningham, M.A. Hoffman, A Comparison of High Pressure and Low Pressure Operation of PEM Fuel Cell Systems, SAE, Detroit MI, March 2001 (paper number 2001-01-0538).
8. D.J. Friedman, Maximizing Direct-Hydrogen Pem Fuel Cell Vehicle Efficiency-Is Hybridization Necessary? SAE 1999 (paper number 1999-01-0530)
9. D.J. Friedman, A. Eggert, P. Badrinarayanan, J.M. Cunningham, Balancing Stack, Air Supply, and Water/Thermal Management Demands for An Indirect Methanol Pem Fuel Cell System, SAE 2001, (paper number 2001-01-0535)
10. F. Barbir, M. Fuchs, A. Husar, J. Neutzler, Design and operational characteristics of automotive PEM fuel cell stacks, SAE 2000 (paper number 2000-01-0011)

11. J.M. Cunningham, M.A. Hoffman, R.M. Moore, D.J. Friedman, Requirements for a Flexible and Realistic Air Supply Model for Incorporation Into a Fuel Cell Vehicle (FCV) System Simulation, SAE 1999, (paper number 1999-01-2912)
12. J. Cunningham, R. Moore, S. Ramaswamy, K.-H. Hauer, A Comparison of Energy Use for a Direct-Hydrogen Hybrid Versus a Direct-Hydrogen, Load-Following Fuel Cell Vehicle, SAE 2003 (paper number 2003-01-0416)
13. S. Gelfi, A.G. Stefanopoulou, J.T. Pukrushpan, H. Peng, Dynamics of Low-Pressure and High-Pressure Fuel Cell Air Supply System, 2003 American Control Conference Denver, ACC2003, Colorado, 2003
14. S. Pischinger, C. Schonfelder, J. Ogrzewalla, Analysis of dynamic requirements for fuel cell systems for vehicle applications, Journal of Power Sources, 154(2), 2006, pp. 420-427
15. J.T. Pukrushpan, A.G. Stefanopoulou, H. Peng, Modeling and Control for PEM Fuel Cell Stack System, Proceedings of the American Control Conference, Anchorage AK, May 2002, pp.3117-3122
16. J.T. Pukrushpan, H. Peng, A.G. Stefanopoulou, Simulation and Analysis of Transient Fuel Cell System Performance Based on a Dynamic Reactant Flow Model, Proceedings of IMECE' 02, 2002 ASME International Mechanical Engineering Congress & Exposition, Nov. 2002
17. C.-J. Sjostedt, J.-G. Persson, The Design of Modular Dynamical Fluid Simulation Systems, OST, Stockholm Sweden, 2005
18. J.T. Pukrushpan, A.G. Stefanopoulou, H. Peng, Control of Fuel Cell Power Systems, Springer, 2004
19. J. Reuter, U.-J. Beister, N. Liu, D. Reuter, B. Eybergen, M. Radhamohan, A. Hutchenreuther, Control of a Fuel Cell Air Supply Module (ASM), SAE 2004 (paper number 2004-01-1009)
20. A. Miotti, A.D. Domenico, Y.G. Guezennec, S. Rajagopalan, Control-oriented model for an automotive PEM fuel cell system with imbedded 1+1D membrane water transport, Vehicle Power and Propulsion, 2005 IEEE Conference, Sept. 2005, pp. 611-618
21. K.-H. Hauer, A. Eggert, R.M. Moore, S. Ramaswamy, The Hybridized Fuel Cell Vehicle Model of the University of California, Davis, SAE 2001, Detroit MI, March 5-8, 2001 (paper number 2001-01-0543)

22. R.M. Moore, K.H. Hauer, D. Friedman, J.M. Cunningham, P. Badrinarayanan, S. Ramaswamy, A. Eggert, A dynamic simulation tool for hydrogen fuel cell vehicles, *Journal of Power Sources*, 141(2) 2005, pp. 272-285
23. J.B. Heywood, *Internal Combustion Engine Fundamentals*, McGraw-Hill, Inc. Appendix C, 1988
24. J.M. Cunningham, R.M. Moore, S. Ramaswamy, A Comparison of Energy Use for a Direct-Hydrogen Hybrid versus a Direct-Hydrogen Load-Following Fuel Cell Vehicle, SAE 2003 (paper number 2003-01-0416)

## Appendix 1

### Unit Conversion Correction of the Former Optimization Model

The pressure drop on the flow path with the square cross-section is derived from the Darcy's Law as in the meter-kilogram-second (MKS) system and centimeter-gram-second (CGS) system.

MKS system

$$\begin{aligned}\Delta P &= f \frac{\text{equiv\_length} \cdot \rho \cdot V^2}{2 \cdot D_{\text{hydraulic}}} \\ &= f \frac{\text{equiv\_length} \cdot \rho \cdot \text{m}^2}{2 \rho D_{\text{hydraulic}}^5} \\ &= f \cdot \frac{m \cdot \left(\frac{kg}{s}\right)^2}{2 \cdot \frac{kg}{m^3} \cdot m^5} \\ &= \frac{f}{2} \cdot \frac{kg \cdot \frac{m}{s^2}}{m^2} \\ &= \frac{f}{2} \cdot \frac{N}{m^2} \quad (Pa)\end{aligned}$$

Mixed MKS/CGS system  
(Used in the optimization model)

$$\begin{aligned}\Delta P &= f \frac{\text{equiv\_length} \cdot \rho \cdot V^2}{2 \cdot D_{\text{hydraulic}}} \\ &= f \frac{\text{equiv\_length} \cdot \rho \cdot \text{m}^2}{2 \rho D_{\text{hydraulic}}^5} \\ &= f \cdot \frac{m \cdot \left(\frac{g}{s}\right)^2}{2 \cdot \frac{g}{cm^3} \cdot cm^5} \\ &= \frac{f}{2} \cdot \frac{g \cdot \frac{m}{s^2}}{cm^2} \\ &= 10 \cdot \frac{f}{2} \cdot \frac{N}{m^2} \quad (Pa)\end{aligned}$$

Instead of using the formula

```
delta_P_test =
ff*mdot_channel^2/2/rho_air/10*equiv_length/D_channel^5/101300; % atm
```

in the original former optimization model, released in 2001, the formula

```
delta_P_test =
ff*mdot_channel^2/2/rho_air*10*equiv_length/D_channel^5/101300; % atm
```

was utilized in the present optimization model. Furthermore, considering the rectangular channel and the pressure drop on the vertical inlet and outlet manifold, the formula was rewritten as

```
delta_P_test = 10*ff*mdot_channel_v^2/2/rho_air*equiv_length...
/width_channel^2/depth_channel^2/D_channel...
/101325*k_DeltaPr;
```

## Appendix 2

### Effect of Humidification on the Mass Flow

In the original fuel cell optimization model, only the dry air mass flow was considered for calculating the pressure drop on the flow field. The effect of the humidification and the oxygen consumption on the air mass flow was not considered (Only the change of the density of the humid air was considered). The saturated water vapor pressure is the function of only temperature and is 0.46733 atm. at 80 °C. The change of the air mass flow caused by humidification is significant and should be considered for calculating the pressure drop on the flow path in the optimization model. The averaged mass flow rate considering the consumed oxygen is employed in the fuel cell system optimization model.

The vapor mass flow is related to the dry air mass flow, the pressure drop and the back pressure according to the ideal gas law. We assume the maximum pressure drop across the stack is 0.4 atm for the optimal model (varying back pressure and varying air stoichiometric ratio operation). The averaged mass flow and pressure are used to calculate the effect of the water vapor mass flow and further the pressure loss.

The following equations are used in the optimization model.

General equations:

$$PV = nRT = m \frac{R}{M} T \quad P_{inlet} = P_{outlet} + \Delta P \quad \dot{m}_{inlet} = \dot{m}_{outlet} + \Delta \dot{m} \quad \Delta P = f \cdot \frac{\dot{m}_{inlet} + \dot{m}_{outlet}}{2}$$

Equations at the inlet of the stack:

$$P_{inlet} = P_{vapor,inlet} + P_{N_2,inlet} + P_{O_2,inlet} \quad \dot{m}_{inlet} = \dot{m}_{vapor,inlet} + \dot{m}_{N_2,inlet} + \dot{m}_{O_2,inlet}$$

$$= P_{vapor,inlet} + P_{air,inlet} \quad = \dot{m}_{vapor,inlet} + \dot{m}_{air,inlet}$$

$$\frac{P_{vapor,inlet}}{P_{air,inlet}} = \frac{n_{vapor,inlet}}{n_{air,inlet}}$$

$$= \frac{m_{vapor,inlet}}{m_{air,inlet}} \cdot \frac{M_{air}}{M_{vapor}}$$

$$= \frac{\dot{m}_{vapor,inlet}}{\dot{m}_{air,inlet}} \cdot \frac{M_{air}}{M_{vapor}}$$

$$\dot{m}_{inlet} = \dot{m}_{vapor,inlet} + \dot{m}_{air,inlet}$$

$$= \frac{P_{vapor,inlet}}{P_{air,inlet}} \cdot \frac{M_{vapor}}{M_{air}} \cdot \dot{m}_{air,inlet} + \dot{m}_{air,inlet}$$

$$= \left( \frac{P_{vapor}}{P_{inlet} - P_{vapor}} \cdot \frac{M_{vapor}}{M_{air}} + 1 \right) \cdot \dot{m}_{air,inlet}$$

Equations at the outlet of the stack:

$$P_{outlet} = P_{vapor,outlet} + P_{N_2,outlet} + P_{O_2,outlet}$$

$$= P_{vapor,outlet} + P_{air,outlet}$$

$$\dot{m}_{outlet} = \dot{m}_{vapor,outlet} + \dot{m}_{N_2,outlet} + \dot{m}_{O_2,outlet}$$

$$= \dot{m}_{vapor,outlet} + \dot{m}_{air,outlet}$$

$$\frac{P_{vapor}}{P_{air,outlet}} = \frac{n_{vapor,outlet}}{n_{air,outlet}}$$

$$= \frac{m_{vapor,outlet}}{m_{air,outlet}} \cdot \frac{M_{air,outlet}}{M_{vapor}}$$

$$= \frac{\dot{m}_{vapor}}{\dot{m}_{air,outlet}} \cdot \frac{M_{air,outlet}}{M_{vapor}}$$

$$\dot{m}_{outlet} = \dot{m}_{vapor,outlet} + \dot{m}_{air,outlet}$$

$$= \frac{P_{vapor}}{P_{air,outlet}} \cdot \frac{M_{vapor}}{M_{air,outlet}} \cdot \dot{m}_{air,outlet} + \dot{m}_{air,outlet}$$

$$= \left( \frac{P_{vapor}}{P_{outlet} - P_{vapor}} \cdot \frac{M_{vapor}}{M_{air,outlet}} + 1 \right) \cdot \dot{m}_{air,outlet}$$

$$\dot{m}_{air,outlet} = \dot{m}_{air,inlet} - \frac{\dot{m}_{air,inlet}}{M_{air,inlet}} \cdot x_{on} \cdot \frac{1}{SR} \cdot M_{O_2}$$

$$= \left( 1 - \frac{x_{on} \cdot M_{O_2}}{SR \cdot M_{air}} \right) \dot{m}_{air,inlet}$$

Oxygen is consumed (reacted) at the cathode. As shown in Figure A2-1, the effect of the consumed oxygen on the change of the dry air mass flow should not be neglected when the SR is less than 2.0. (Usually the optimal SR from the optimization model is less than 2.)

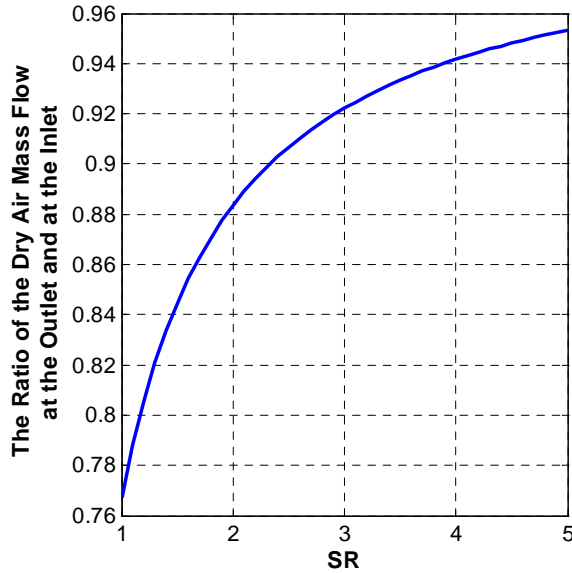


Figure A2-1 Change of the air mass flow after reaction vs. SR

The molecular weight of the exhaust dry air can be expressed as

$$M_{air,outlet} = \frac{x_{on} \frac{SR-1}{SR}}{1 - x_{on} \frac{1}{SR}} M_{O_2} + \frac{1 - x_{on}}{1 - x_{on} \frac{1}{SR}} M_{N_2}$$

and is plotted in Figure A2-2

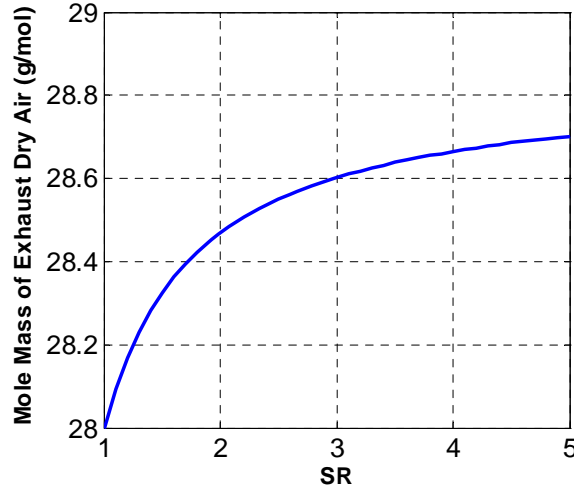


Figure A2-2 Change of the dry air mole mass after reaction vs. SR

The curve shows the change of the molecular weight of the exhaust dry air changes with the change of the SR. However, the change of the mole mass is less than 2 percent and can be neglected in the optimization model when the SR is less than 2. We assume

$$M_{air,outlet} \cong M_{air,inlet} = M_{air}$$

The average mass flow can be expressed as

$$\begin{aligned} \dot{m}_{average} &= \frac{\dot{m}_{inlet} + \dot{m}_{outlet}}{2} \\ &= \frac{1}{2} \left[ \left( \frac{P_{vapor}}{P_{inlet} - P_{vapor}} \cdot \frac{M_{vapor}}{M_{air}} + 1 \right) \cdot \dot{m}_{air,inlet} + \left( \frac{P_{vapor}}{P_{outlet} - P_{vapor}} \cdot \frac{M_{vapor}}{M_{air,outlet}} + 1 \right) \cdot \dot{m}_{air,outlet} \right] \\ &= \frac{1}{2} \left[ \left( \frac{P_{vapor}}{P_{inlet} - P_{vapor}} \cdot \frac{M_{vapor}}{M_{air}} + 1 \right) \cdot \dot{m}_{air,inlet} + \left( \frac{P_{vapor}}{P_{outlet} - P_{vapor}} \cdot \frac{M_{vapor}}{M_{air}} + 1 \right) \cdot \dot{m}_{air,outlet} \right] \\ &= \frac{1}{2} \left[ \left( \frac{P_{vapor}}{P_{inlet} - P_{vapor}} \cdot \frac{M_{vapor}}{M_{air}} + 1 \right) + \left( \frac{P_{vapor}}{P_{outlet} - P_{vapor}} \cdot \frac{M_{vapor}}{M_{air}} + 1 \right) \cdot \left( 1 - \frac{x_{on} \cdot M_{O_2}}{SR \cdot M_{air}} \right) \right] \cdot \dot{m}_{air,inlet} \end{aligned}$$

In most cases, the pressure drop in the vertical inlet/outlet manifolds is less than a one-quarter of the pressure drop in the flow channels of the stack. The flow in the channels is

laminar for the flow velocity and the channel design of interest for fuel cells. If it is assumed that the flow in the channels fully developed, steady, and incompressible flow, the Darcy-Weisbach equation is valid and the pressure drop is expressed as

$$\Delta P = \lambda \frac{L\rho v^2}{2D_h}$$

where  $\lambda$  is the friction coefficient,  $\rho$  is the average humid air density which is a function of pressure, humidity, and temperature,  $v$  is the flow velocity, and  $L$  and  $D_h$  are the equivalent length and hydraulic diameter of the channels, respectively.

For fully developed laminar flow, the roughness of the flow paths can be neglected. The friction coefficient depends on the Reynolds Number  $R_e$  and can be expressed as

$$\lambda = \frac{64}{R_e} = \frac{64\mu}{D_h v \rho}$$

where  $R_e$  is the Reynolds number, and  $\mu$  is the dynamic or absolute viscosity. The pressure drop across the stack can be rewritten as

$$\Delta P = \frac{32\mu L}{D_h^2} \frac{\dot{m}_{ch}}{\rho A_{ch}} k$$

where  $\dot{m}_{ch}$  is the mass flow rate in the flow channel,  $A_{ch}$  is the cross section area of the flow channel, and  $k$  is the correction coefficient for the pressure loss on the vertical inlet/outlet manifold. The outlet mass flow and pressure drop relationship becomes

$$\dot{m}_{ch} = \frac{\rho A_{ch} D_h^2}{32\mu L k} \Delta P$$

## Appendix 3

### Change of the Air SR Calculation in the Quasi-Steady Fuel Cell System

DHFCV\_load/vehicle/fuel cell system/Air Supply System/Output Data

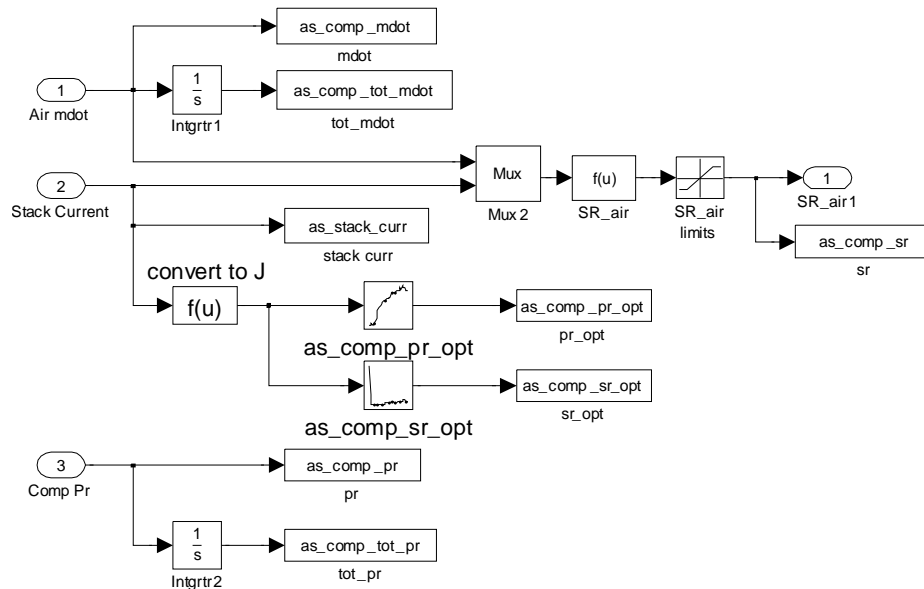


Figure A3-1 Block diagram of the SR calculation in the DHFC model

The formula

$$SR_{air} = u[1]/n_{cell} * 4 * F / (u[2] * 4.76 * MW_{air} + 0.1)$$

for calculating the air stoich. ratio in the DHFC model was replaced by the formula

$$SR_{air} = u[1]/n_{cell} * 4 * F * X_{on} / u[2] / MW_{air}$$

which is derived from the following equations

$$x_{on} = \frac{n_{O_2}}{n_{Air}} = \frac{m_{O_2} / M_{O_2}}{m_{air} / M_{air}} = \frac{\dot{m}_{O_2} / M_{O_2}}{\dot{m}_{air} / M_{air}}$$

$$\dot{m}_{O_2} = \frac{M_{O_2}}{M_{air}} x_{on} \dot{m}_{air}$$

$$\dot{m}_{O_2,react} = \frac{n_{cell}}{4F} I \cdot M_{O_2}$$

$$SR = \frac{\dot{m}_{O_2}}{\dot{m}_{O_2,react}} = \frac{4 \cdot F \cdot x_{on} \cdot \dot{m}_{air}}{M_{air} \cdot I \cdot n_{cell}}$$

Or air SR can be obtained by a lookup table of optimal SR indexed by the current density. The block diagram of the SR calculation is shown in Figure A3-1.

## Appendix 4

### Traction Motor Controller

A resettable PI controller is used in the traction motor controller, as shown in Figure A4-11. The integral component of the torque command can be reset by the brake pedal position signal. Compared to the former motor controller as shown in Figure A4-22, the resettable PI controller can smooth the power request while keeping the vehicle speed following the drive cycle profile.

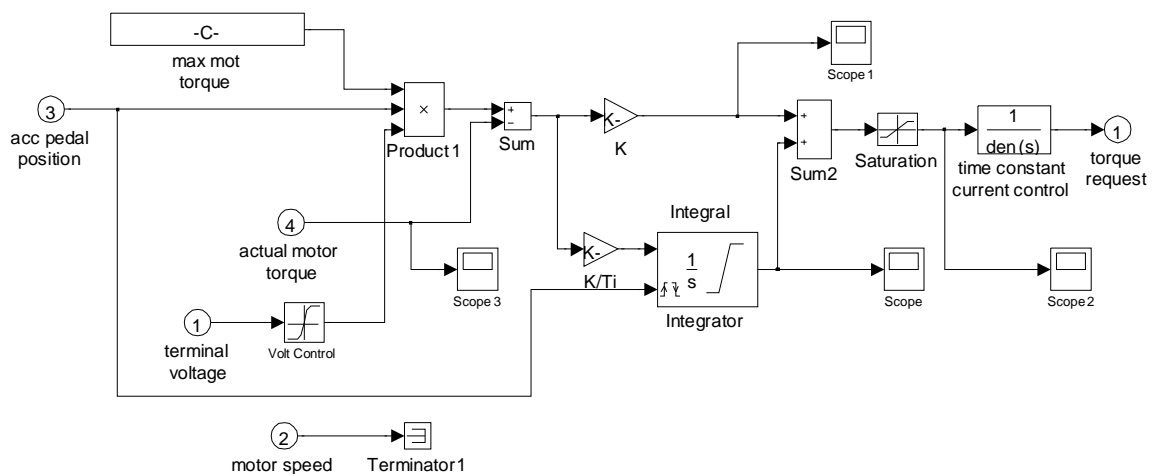


Figure A4-1 A resettable PI controller for the traction motor

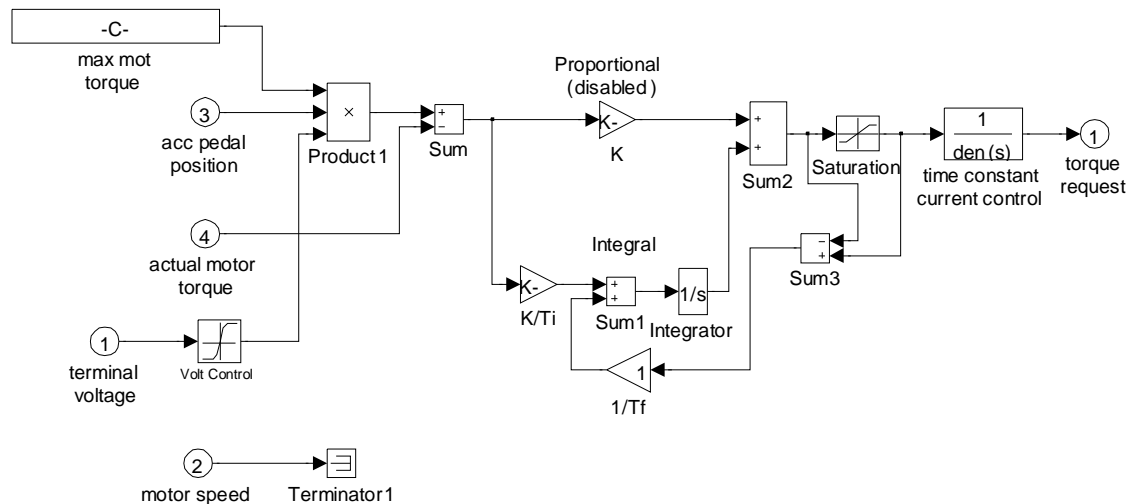


Figure A4-2 Block diagram of the traction motor controller in the former FCVMP

## Appendix 5

### ***Operation Instructions for Fuel Cell System and Fuel Cell Vehicle Models***

The model directory and subdirectory are

Fuel cell system optimization model

```
FCS_Steady_2008\  
  \FCSSteadyData\  
  \FCSSteadyGUI\  
  \FCSSteadyModel\  
  \s1.m
```

s1.m is the main run file to load the quasi-steady state optimization model GUI. Sizing of the fuel cell system and optimization of the operating conditions can be achieved through GUI. The results from this model can be directly applied to the dynamic fuel cell system model and the direct hydrogen fuel cell vehicle models.

Fuel cell system dynamic model

```
FCS_Dynamic_2008\  
  \FCSDynamicAppl\  
  \FCSDynamicData\  
  \f1.m  
  \d1.m
```

f1.m is the run file to reshape and reverse the performance map of a twinscrew compressor, and generate and treat the input weights and layer weights and biases of the neural network.

d1.m is the run file to run the dynamic fuel cell system model. This model is used to verify the stability of the system and tune control parameters. The results will be used in the fuel cell vehicle model along with the optimal operating conditions.

Fuel cell vehicle model with quasi-steady state fuel cell system model

```
FCVMP_Steady_2008\  
  \ucd_dhfc\  
  \Optimal_Data_FCS\  
  \ucd_allvehicle.m
```

Fuel cell vehicle model with dynamic fuel cell system model

```
FCVMP_Dynamic_2008\  
  \ucd_dhfc\  
  \Optimal_Data_FCS\  
  \ucd_allvehicle.m
```

ucd\_allvehicle.m is the main run file for the fuel cell vehicle model. DHFC is the only fuel cell vehicle model with a dynamic fuel cell system model.

## Tables of Figures

Figure 1 Direct hydrogen fuel cell system Schematic Diagram .....	4
Figure 2 Diagram of the fuel cell system for direct hydrogen fuel cell vehicles.....	5
Figure 3 Driver end of the direct hydrogen fuel cell vehicle model.....	5
Figure 4 Interface of the fuel cell system optimization model .....	7
Figure 5 Mass flow ratio of the outlet and inlet dry air flow vs. SR .....	10
Figure 6 Outlet flow dry air mole mass vs. SR.....	11
Figure 7 Flowchart of searching for the optimum operating conditions for the varying air stoich. number varying back pressure operation.....	13
Figure 8 Optimum operating conditions for a direct hydrogen fuel cell system .....	14
Figure 9 Comparison of the system efficiency for different operating modes: optimal varying back pressure operation and fixed back pressure of 2.0, 1.5, and 1.1 atm. ....	15
Figure 10 Optimal fuel cell polarization curves for different operating modes .....	16
Figure 11 Compressor quasi-steady responses for different operating modes .....	16
Figure 12 Fuel cell system net power vs. current density.....	17
Figure 13 Stack gross power vs. current density .....	17
Figure 14 Air supply stoich. ratio vs. current density.....	18
Figure 15 Dry air mass flow vs. current density.....	18
Figure 16 Pressure drop across the stack vs. current density.....	19
Figure 17 Oxygen partial pressure at the catalyst layer vs. current density .....	19
Figure 18 Diagram of the dynamic fuel cell system model (Air supply) .....	21
Figure 19 Compressor speed calculation .....	22
Figure 20 Diagram of compressor drive motor control .....	22
Figure 21 Diagram of compressor and drive motor performance.....	23
Figure 22 Neural net work for the mass flow rate calculation.....	23
Figure 23 Block diagram of the supply manifold.....	25
Figure 24 Block diagram of the Cooler and Humidifier.....	26
Figure 25 Diagram of the back pressure throttle and control .....	27
Figure 26 Diagram for the oxygen partial pressure calculation.....	28
Figure 27 Block diagram of the fuel cell model .....	28
Figure 28 Transient response of the fuel cell system under a series of step current.....	30
Figure 29 Simulation results of system power flow and efficiency.....	31
Figure 30 Performance control response of the compressor.....	32
Figure 31 Comparison of current-voltage trajectory from the dynamic model and the quasi-steady optimization model .....	32
Figure 32 Pressure responses of the supply manifold, fuel cell cathode, and the return manifold .....	33
Figure 33 Mass flow trajectory of the compressor outlet flow (dry air) and the fuel cell inlet flow (fully humidified air) under the step current .....	33
Figure 34 Comparison of the transient response of the system with a closed-loop control of the mass flow rate and without a feedback mass flow control (feed forward control only) .....	34

Figure 35 Simulation results of the DHFC vehicle with the dynamic fuel cell system model on the FUDS cycle.....	35
Figure 36 Simulation results of the DHFC vehicle with quasi-steady state fuel cell system model on the FUDS cycle.....	36
Figure 37 Comparison of the system performance with the quasi-steady and dynamic fuel cell system model on FUDS drive cycle.....	36
Figure 38 Fuel economy (gasoline equivalent) of the DHFC vehicle with the quasi-steady state and with dynamic fuel cell system model on different driving cycles (Case 1).....	37
Figure 39 Fuel economy of the DHFC vehicle operating at optimal back pressures and fixed back pressures of 2.0, 1.5, and 1.1 atm. on different driving cycles (Case 1).....	38
Figure 40 Fuel economy of the DHFC vehicle with a smaller fuel cell system operating at optimal back pressures and fixed back pressures of 2.0, 1.5, and 1.1 atm. on different driving cycles (Case 2).....	39
Figure 41 Normalized fuel economy of the DHFC vehicle (case 2: a small fuel cell system) to the DHFC vehicle (case 1) .....	39

## Tables

Table 1 Fuel cell stack and system parameters.....	15
Table 2 Fuel cell system parameters (case 1) .....	29
Table 3 Vehicle and fuel cell system parameters (Case 1) .....	37
Table 4 Vehicle and fuel cell system parameters (Case 2) .....	38